Key Points:
- Numerical methods developed for bimaterial earthquake cycles
- Material mismatch affects rupture direction
- Preferred rupture favorable with bimaterial properties

Correspondence to:
B. A. Erickson,
berickson@pdx.edu

Bimaterial effects in an earthquake cycle model using rate-and-state friction

Brittany A. Erickson[1] and Steven M. Day[2]

[1]Department of Mathematics and Statistics, Portland State University, Portland, Oregon, USA, [2]Department of Geological Sciences, San Diego State University, San Diego, California, USA

Abstract We have developed a computational framework to study earthquake cycles in 2-D plane strain and apply it to faults separating dissimilar material. We consider a planar, strike-slip fault governed by rate-and-state friction where quasi-dynamic events nucleate spontaneously due to remote, tectonic loading. We investigate the influence of material contrast over the course of many hundreds of years. For the parameters we consider, we find that the presence of bimaterial properties influences the earthquake nucleation site, such that rupture in the preferred direction (that is, in the direction of particle motion of the side of the fault with lower shear wave velocity) is favorable. For large values of the critical slip distance D_c, events propagating in the preferred rupture direction occur for a wide range of material contrasts. For smaller values of D_c, small events emerge, even in the monomaterial case. With material mismatch present, some of these small events propagate in the nonpreferred direction, made possible by a favorable stress distribution left on the fault from previous ruptures. These results may shed light on our understanding of rupture directivity on large strike-slip faults (like the San Andreas Fault in California) which occasionally host events rupturing in the nonpreferred direction.

1. Introduction

Natural faults separate rocks with heterogeneous material properties. Examples include strike-slip faults where large total displacements juxtapose differing lithologies with variable elastic properties [*Allam et al.*, 2014], subduction zones joining continental and oceanic crustal blocks, and stick-slip motion of glaciers at the interface of ice and underlying bedrock [e.g., *Weertman*, 2005; *Danesi et al.*, 2007]. It has been speculated that material mismatch across a fault may be important for the interpretation of geodetic data across faults [*Le Pichon et al.*, 2005; *Fialko*, 2006] and may be responsible for rupture directivity. Theoretical considerations predict that while slip on a planar fault separating similar material induces no changes in normal stress, material mismatch produces an asymmetric normal stress change [*Weertman*, 1980; *Andrews and Ben-Zion*, 1997] that might cause rupture to propagate in the "preferred" direction (the direction of particle motion of the side with slower shear wave velocity). Both laboratory studies and dynamic rupture simulations on a bimaterial fault interface, however, show that material mismatch produces an asymmetry in rupture, not always confined to the preferred direction [*Anooshehpoor and Brune*, 1999; *Harris and Day*, 1997; *Andrews and Ben-Zion*, 1997; *Ben-Zion and Andrews*, 1998; *Ben-Zion and Huang*, 2002; *Xia et al.*, 2005; *Harris and Day*, 2005]. The studies of *Andrews and Harris* [2005], however, suggest that rupture propagation is dominated by stress heterogeneity rather than bimaterial effects, at least in 3-D simulations. Field observations also reveal a variety of rupture styles and directions on faults separating dissimilar material [*Rubin and Gillard*, 2000; *Dor et al.*, 2006, 2008; *Kane et al.*, 2013], suggesting that bimaterial effects alone probably do not determine rupture directivity. Because increased ground motion damage and triggered seismicity are often observed in the forward direction of rupture [see *Harris and Day*, 2005, and references therein], an understanding of rupture direction would be helpful in improving seismic hazard estimates.

Although rupture asymmetry is predicted from theoretical considerations, how bimaterial properties influence the earthquake cycle in nature is unclear due to the fact that natural faults can host ruptures in the nonpreferred direction. For example, *Harris and Day* [2005] studied eight magnitude 4–6 earthquakes that occurred on the San Andreas Fault at Parkfield since 1934, three of which propagated in the preferred direction (to the SE) and five that propagated to the NW (including the M_6 2004 event). They concluded that these data do not support the preferred rupture direction that could be inferred from rock compliance contrasts but may be more controlled by fault geometry and rheology. What controls rupture direction is still a debated topic

[see *Ben-Zion*, 2006; *Harris and Day*, 2006] and recent detailed structural imaging studies indicate that there exist variations in the fault velocity contrast (including a reversal in the sense of contrast near the hypocenter of the 2004 event) that might help explain the observed rupture direction [*Zhao et al.*, 2010; *Bennington et al.*, 2013]. In a recent study of 450 small earthquakes at Parkfield, *Kane et al.* [2013] showed a roughly equal number of events propagating to the SE and NW and only saw greater rupture directivity in the preferred direction (70% SE) if they limited their data sets to those earthquakes of larger magnitudes.

Many numerical studies of dynamic ruptures have shown that the presence of bimaterial properties can lead to a preferred rupture direction as well as asymmetric rupture features (sometimes propagating uni-laterally), a preferred aftershock triggering and asymmetric off-fault damage [*Shi and Ben-Zion*, 2006; *Rubin and Ampuero*, 2007; *Ampuero and Ben-Zion*, 2008; *Duan*, 2008; *Brietzke et al.*, 2009; *Dalguer and Day*, 2009; *DeDontney et al.*, 2011]. For example, *Rubin and Ampuero* [2007] used dynamic models of slip weakening in rupture on bimaterial faults in order to understand the observed asymmetric distribution of microearthquake aftershocks along the central San Andreas Fault. They observed subshear ruptures growing as slightly asymmetric, bilateral cracks, with larger velocities and normal stress changes in the preferred direction. They argue that the residual stresses left behind after the rupture terminates at the two stress barriers on either end of the fault may be such that the SE side is far below the failure threshold, whereas the NW remains quite close to failure. This residual stress may be partially responsible for the observed aftershock asymmetry. *Ampuero and Ben-Zion* [2008] studied in-plane ruptures on bimaterial faults governed by velocity-weakening friction and characterize ranges of velocity-weakening scales, nucleation lengths, and background stresses that give rise to pulse or crack, bilateral or unilateral, and dying or sustained pulses. Ruptures propagating in the non-preferred direction were also possible but dependent on statistical properties of the heterogeneous, initial background stress assumed. These conclusions give insight into how rupture in the nonpreferred direction could be possible due to residual stresses left by past earthquakes but rely on making a priori assumptions about the background stress.

Many of the conclusions drawn from the dynamic rupture simulations depend on the initial background stress and the employed nucleation procedure necessary to initiate rupture. This procedure generates artificial initial conditions sufficient to immediately nucleate rupture, but it is unclear what part the bimaterial effect plays out over multiple earthquake cycles that develop naturally. In this work we study the influence of material mismatch on the earthquake cycle where quasi-dynamic ruptures nucleate spontaneously in response to remote tectonic loading.

In the current study, a planar, strike-slip fault interface separates elastically dissimilar materials and is governed by rate-and-state friction with strike-variable frictional properties [*Dieterich*, 1979; *Ruina*, 1983; *Marone*, 1998]. To introduce the problem, we first describe in section 2 the classical 2-D plane strain equations governing motion in the domain as well as the corresponding boundary conditions that we use to impose remote tectonic loading. We employ a provably stable finite difference method satisfying a summation-by-parts (SBP) rule to discretize the off-fault material, and all interface and boundary conditions are imposed weakly through the simultaneous-approximation-technique (SAT) [*Mattsson and Nordström*, 2004; *Duru and Virta*, 2014]. Details of the fault interface treatment are described in section 3, with specifics of the friction law detailed in section 4. Our time-stepping technique is detailed in section 5, and we show convergence results in section 6. Results from our application simulations are detailed in section 7, and a discussion is given in section 8.

2. Homogeneous Material Problem With No Fault Interface

To better describe the computational framework, we will first look at the 2-D plane strain equations without reference to a fault interface and assume homogeneous material properties. We address faults separating different elastic materials in section 3. We will review the analysis showing that the continuous equations and boundary conditions provide an energy estimate that leads to a provably stable discretization for our numerical studies.

2.1. Continuous Formulation and Energy Estimate

Consider the rectangular domain $\Omega = [0, L_x] \times [-L_y/2, L_y/2]$ and let u and w denote the horizontal and vertical components of the displacement vector $\vec{U} = (u, w)$, see Figure 1. The 2-D plane strain equations governing
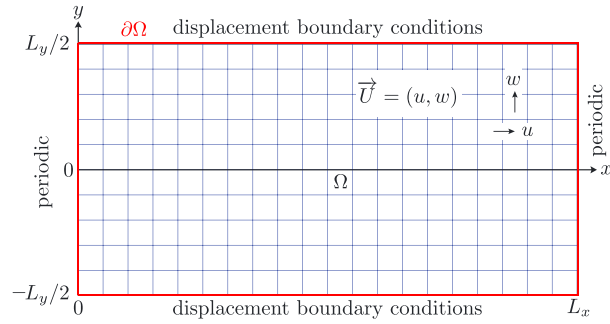
Figure 1. Problem geometry for single domain Ω with no interface. At the boundaries, denoted $\partial\Omega$, we consider both Dirichlet (displacement) and periodic boundary conditions. The displacement vector $\vec{U}$ has components u (displacement in the horizontal direction) and w (displacement in the vertical direction).

motion in the domain are given by

$$\rho u_{tt} = \frac{\partial}{\partial x}\sigma_{xx} + \frac{\partial}{\partial y}\sigma_{xy} \tag{1a}$$

$$\rho w_{tt} = \frac{\partial}{\partial x}\sigma_{xy} + \frac{\partial}{\partial y}\sigma_{yy}, \quad (x,y) \in \Omega \tag{1b}$$

where the stresses are

$$\sigma_{xx} = (\lambda + 2\mu)\frac{\partial u}{\partial x} + \lambda\frac{\partial w}{\partial y} \tag{2a}$$

$$\sigma_{xy} = \mu(\frac{\partial u}{\partial y} + \frac{\partial w}{\partial x}) \tag{2b}$$

$$\sigma_{yy} = \lambda\frac{\partial u}{\partial x} + (\lambda + 2\mu)\frac{\partial w}{\partial y} \tag{2c}$$

$$\sigma_{zz} = \lambda(\frac{\partial u}{\partial x} + \frac{\partial w}{\partial y}). \tag{2d}$$

The elastic moduli λ, μ, and ρ are Lamé's first parameter, the shear modulus, and the material density, respectively. The shear and longitudinal wave speeds are given by $c_s = \sqrt{\mu/\rho}$ and $c_p = \sqrt{(\lambda + 2\mu)/\rho}$, and we will refer in future sections to Poisson's ratio $\nu = \lambda/[2(\lambda + \mu)]$.

Assuming homogenous material properties within the domain, substitution of (1) into (2) yields the elastodynamic wave equation for 2-D plane strain:

$$\rho u_{tt} = (\lambda + 2\mu)\frac{\partial^2 u}{\partial x^2} + (\mu + \lambda)\frac{\partial^2 w}{\partial x \partial y} + \mu\frac{\partial^2 u}{\partial y^2} \tag{3a}$$

$$\rho w_{tt} = \mu\frac{\partial^2 w}{\partial x^2} + (\mu + \lambda)\frac{\partial^2 u}{\partial x \partial y} + (\lambda + 2\mu)\frac{\partial^2 w}{\partial y^2} \quad (x,y) \in \Omega. \tag{3b}$$

The governing equation (3) must be supplied boundary conditions on $\partial\Omega$. In this work we consider conditions on the displacement vector $\vec{U}$ at $y = L_y/2$ and $y = -L_y/2$ (the upper and lower boundaries, see Figure 1). At the left and right boundaries we impose periodic conditions which enforce continuity conditions in the components of $\vec{U}$ as well as on the traction vector $\vec{T} = (\sigma_{xj}n_j, \sigma_{yj}n_j)$, where $\vec{n} = (n_1, n_2)$ is the unit outward facing normal vector (in 2-D) from the boundary. The boundary conditions we enforce are given by

$$(\text{bottom}) \quad u(t, x, -L_y/2) = g_B(t, x), \quad w(t, x, -L_y/2) = h_B(t, x), \tag{4a}$$

$$\text{(top)} \quad u(t,x,L_y/2) = g_T(t,x), \quad w(t,x,L_y/2) = h_T(t,x), \tag{4b}$$

$$\text{(periodic at left/right)} \quad u(t,L_x,y) - u(t,0,y) = 0, \tag{4c}$$

$$w(t,L_x,y) - w(t,0,y) = 0, \tag{4d}$$

$$\sigma_{xx}(t,L_x,y) - \sigma_{xx}(t,0,y) = 0, \tag{4e}$$

$$\sigma_{xy}(t,L_x,y) - \sigma_{xy}(t,0,y) = 0, \tag{4f}$$

where $g_B, h_B, g_T,$ and h_T are the given data to be enforced at the bottom and top boundaries (denoted with subscripts B and T). For example, we will later impose slow loading at the top and bottom boundaries by assuming $g_T = V_p t/2$ and $g_B = -V_p t/2$, where $V_p \approx 32$ mm/a is a slow plate rate.

To show that the initial-boundary-value problem (3) and (4) (along with suitable initial conditions) specify a well-posed problem can be done through the so-called energy method. Although the following analysis of the continuous problem is well known, we include it here for clarity when describing the discretized equations (which mimic the energy estimate for the continuous problem). The continuous energy for equation (3) (and analogously for (1) and (2)) is defined as

$$E = \int_{-L_y/2}^{L_y/2} \int_0^{L_x} \frac{\rho}{2}(u_t^2 + w_t^2) + \frac{1}{4\mu}\sigma_{ij}\left(\sigma_{ij} - \frac{\lambda}{3\lambda + 2\mu}\sigma_{kk}\delta_{ij}\right) \mathrm{d}x\mathrm{d}y. \tag{5}$$

Taking the time derivative of (5) yields

$$\dot{E} = \int_{-L_y/2}^{L_y/2} \int_0^{L_x} \rho(u_t u_{tt} + w_t w_{tt}) + \frac{\mathrm{d}}{\mathrm{d}t}\left[\frac{1}{4\mu}\sigma_{ij}\left(\sigma_{ij} - \frac{\lambda}{3\lambda + 2\mu}\sigma_{kk}\delta_{ij}\right)\right] \mathrm{d}x\mathrm{d}y. \tag{6}$$

Substituting the governing equations (1) into (6) and integrating the first two terms by parts leave only the terms on the boundary so that

$$\dot{E} = \int_{-L_y/2}^{L_y/2} u_t \sigma_{xx}\Big|_0^{L_x} \mathrm{d}y + \int_0^{L_x} u_t \sigma_{xy}\Big|_{-L_y/2}^{L_y/2} \mathrm{d}x + \int_{-L_y/2}^{L_y/2} w_t \sigma_{xy}\Big|_0^{L_x} \mathrm{d}y + \int_0^{L_x} w_t \sigma_{yy}\Big|_{-L_y/2}^{L_y/2} \mathrm{d}x = \oint \dot{U}_i \sigma_{ij} n_j, \tag{7}$$

where $\dot{U} = (u_t, w_t)$ is the vector of particle velocities. For simplicity in the analysis only (see Appendix A in *Erickson and Dunham* [2014] for a discussion), we may take the boundary data $g_B = h_B = g_T = h_T = 0$, so that (7) reduces to

$$\dot{E} = 0, \tag{8}$$

which shows conservation of energy (in the absence of nonzero boundary data and source terms). This analysis is mimicked in the next section to derive a stable numerical discretization.

2.2. Semidiscrete Formulation and Energy Estimate

We discretize equation (3) using the narrowband summation-by-parts (SBP) operators for second derivatives from *Mattsson and Nordström* [2004] and *Mattsson* [2011] and detailed in *Erickson and Dunham* [2014]. Assuming $N_x + 1$ grid points in the x direction and $N_y + 1$ in the y direction, the grid spacing is given by $\Delta x = L_x/N_x, \Delta y = L_y/N_y$. We let the bold notation $\mathbf{u}, \mathbf{w}$ now stand for the grid vectors approximating the components of the displacement vector solution such that

$$\mathbf{u} = [\mathbf{u_0} \ \mathbf{u_2} \ ... \ \mathbf{u_{N_x}}]^T \tag{9}$$

where

$$\mathbf{u_i} = [u_{i,0}, \ u_{i,1}, \ ... \ u_{i,N_y}], \quad i = 0, ..., N_x \tag{10}$$

and $u_{i,j} \approx u(t, x_i, y_j)$ and $w_{i,j} \approx w(t, x_i, y_j)$. Note that implicit in this notation is that the grid vectors and their components are continuous functions of time in this semidiscrete analysis, e.g., $\mathbf{u} = \mathbf{u}(t)$, $u_{i,j} = u_{i,j}(t)$.

Given a 1-D SBP finite difference operator for first derivatives $\mathbf{D} \approx \partial/\partial x$, the narrowband second derivative operator is given by

$$\frac{\partial^2}{\partial x^2} \approx \mathbf{H}^{-1}(-\mathbf{A} + \mathbf{BS}), \quad \text{where} \quad \mathbf{A} = \mathbf{D}^T\mathbf{HD} + \mathbf{R} \tag{11}$$

[*Mattsson and Nordström*, 2004]. Matrix $\mathbf{H}$ is a symmetric, positive-definite matrix used to define a discrete norm, and $\mathbf{R}$ is a positive-definite damping matrix. Matrix $\mathbf{S}$ is constructed to give an approximation to the first derivative at the boundaries and matrix $\mathbf{B} = \text{diag}[-1, 0, \quad, 0, 1]$. These matrices are all $N_x + 1 \times N_x + 1$ square matrices detailed in *Erickson and Dunham* [2014]. The 2-D operators are then obtained by use of the Kronecker product, which is defined as follows. If $\mathbf{V}$ is an $m \times n$ matrix and $\mathbf{W}$ is a $p \times q$ matrix, then their Kronecker product is an $mp \times nq$ matrix defined by

$$\mathbf{V} \otimes \mathbf{W} = \begin{bmatrix} v_{11}\mathbf{W} & \dots & v_{1n}\mathbf{W} \\ \vdots & \ddots & \vdots \\ v_{m1}\mathbf{W} & \dots & v_{mn}\mathbf{W} \end{bmatrix}.$$

Thus, the 2-D operators are given by

$$\frac{\partial^2}{\partial x^2} \approx \mathbf{H}^{-1}(-\mathbf{A} + \mathbf{BS}) \otimes \mathbf{I} \quad \text{and} \quad \frac{\partial^2}{\partial y^2} \approx \mathbf{I} \otimes \mathbf{H}^{-1}(-\mathbf{A} + \mathbf{BS}), \tag{12}$$

where $\mathbf{I}$ is the identity matrix whose size can be understood by the following. In our notation, a 2-D operator $\mathbf{P} = \mathbf{P}_1 \otimes \mathbf{P}_2$ is written as the Kronecker product of two 1-D operators ($\mathbf{P}_1$ is of size $N_x + 1 \times N_x + 1$, and $\mathbf{P}_2$ is of size $N_y + 1 \times N_y + 1$, respectively), so the notational ordering of the product reflects its size. The discrete L^2 norm on the space of grid functions is thus given by

$$||\mathbf{u}||_{\mathbf{H}}^2 = \mathbf{u}^T(\mathbf{H} \otimes \mathbf{H})\mathbf{u} \tag{13}$$

and the first derivatives in 2-D are approximated by

$$\frac{\partial}{\partial x} \approx \mathbf{D} \otimes \mathbf{I}, \quad \frac{\partial}{\partial y} \approx \mathbf{I} \otimes \mathbf{D}. \tag{14}$$

We discretize (3) (in space) by

$$\rho\mathbf{u}_{tt} = (\lambda + 2\mu)[\mathbf{H}^{-1}(-\mathbf{A} + \mathbf{BS}) \otimes \mathbf{I}]\mathbf{u} + (\mu + \lambda)(\mathbf{D} \otimes \mathbf{D})\mathbf{w} + \mu(\mathbf{I} \otimes \mathbf{H}^{-1}(-\mathbf{A} + \mathbf{BS}))\mathbf{u} + \mathbf{P}_1 \tag{15a}$$

$$\rho\mathbf{w}_{tt} = \mu(\mathbf{H}^{-1}(-\mathbf{A} + \mathbf{BS}) \otimes \mathbf{I})\mathbf{w} + (\mu + \lambda)(\mathbf{D} \otimes \mathbf{D})\mathbf{u} + (\lambda + 2\mu)(\mathbf{I} \otimes \mathbf{H}^{-1}(-\mathbf{A} + \mathbf{BS}))\mathbf{w} + \mathbf{P}_2. \tag{15b}$$

The discrete stresses are given by

$$\sigma_{xx} = (\lambda + 2\mu)(\mathbf{D} \otimes \mathbf{I})\mathbf{u} + \lambda(\mathbf{I} \otimes \mathbf{D})\mathbf{w} \tag{16a}$$

$$\sigma_{xy} = \mu(\mathbf{I} \otimes \mathbf{D})\mathbf{u} + \mu(\mathbf{D} \otimes \mathbf{I})\mathbf{w} \tag{16b}$$

$$\sigma_{yy} = \lambda(\mathbf{D} \otimes \mathbf{I})\mathbf{u} + (\lambda + 2\mu)(\mathbf{I} \otimes \mathbf{D})\mathbf{w} \tag{16c}$$

$$\sigma_{zz} = \lambda(\mathbf{D} \otimes \mathbf{I})\mathbf{u} + \lambda(\mathbf{I} \otimes \mathbf{D})\mathbf{w}. \tag{16d}$$

The SAT penalty vectors $\mathbf{P}_1$ and $\mathbf{P}_2$ in (15) depend on six penalty parameters (detailed Appendix A) and enforce the boundary conditions (4) weakly. The values for the penalty parameters are chosen in such a way such
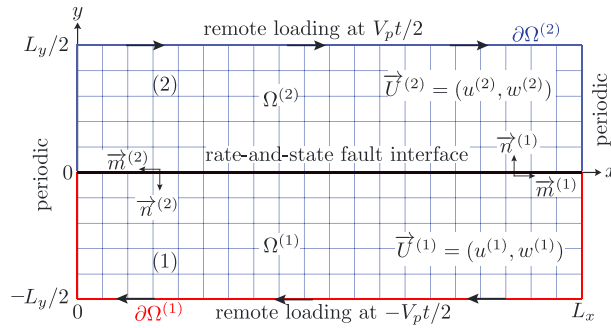
Figure 2. Problem geometry, similar to that in Figure 1 but with a flat fault interface at $y = 0$, governed by rate-and-state friction. Remote loading occurs at the top and bottom boundaries, with periodic boundaries at the left and right.

that the semidiscrete energy mimics the continuous energy (5). The semidiscrete energy (the analog of (5)) is given by

$$\mathbf{E} = \frac{\rho}{2}\left(\mathbf{u}_t^T(\mathbf{H}\otimes\mathbf{H})\mathbf{u}_t + \mathbf{w}_t^T(\mathbf{H}\otimes\mathbf{H})\mathbf{w}_t\right) + \frac{1}{4\mu}\sigma_{ij}^T(\mathbf{H}\otimes\mathbf{H})(\sigma_{ij} - \frac{\lambda}{3\lambda+2\mu}\sigma_{kk}\delta_{ij}) + \hat{\mathbf{d}} \tag{17}$$

where the damping term $\hat{\mathbf{d}}$ comes from the narrowband second derivative operators and goes to 0 as $\Delta x, \Delta y \to 0$ (see Appendix A). *Duru and Virta* [2014] derive conditions on the penalty parameters enforcing the periodic boundary conditions (a specific case of the interface treatment) and show that substitution of the semidiscrete equations (15) into the time derivative of (17) mimics the continuous energy estimate (8), see Appendix A. These conditions ensure that

$$\dot{\mathbf{E}} \leq 0. \tag{18}$$

Thus, (15) is a stable approximation to (3) and (4).

3. Bimaterial Problem With Fault Interface

We will now look at the bimaterial problem, where a fault interface separates elastically dissimilar material, see Figure 2. We will first describe the continuous equations governing motion on either side of the fault, as well as the fault interface conditions that couple the equations together, followed by a description of the semidiscrete problem.

3.1. Continuous Formulation and Energy Estimate

We consider the two subdomains in Figure 2, where $\Omega^{(1)} = [0, L_x] \times [-L_y/2, 0]$ and $\Omega^{(2)} = [0, L_x] \times [0, L_y/2]$. We let u and w denote the horizontal and vertical components of the displacement vector $\vec{U}^{(l)} = (u^{(l)}, w^{(l)})$ where the superscript $(l), l = 1, 2$ refers to the particular side of the fault. The 2-D plane strain equations governing motion in both subdomains are given by

$$\rho u_{tt}^{(l)} = (\lambda^{(l)} + 2\mu^{(l)})\frac{\partial^2 u^{(l)}}{\partial x^2} + (\mu^{(l)} + \lambda^{(l)})\frac{\partial^2 w^{(l)}}{\partial x \partial y} + \mu^{(l)}\frac{\partial^2 u^{(l)}}{\partial y^2} \tag{19a}$$

$$\rho w_{tt}^{(l)} = \mu^{(l)}\frac{\partial^2 w^{(l)}}{\partial x^2} + (\mu^{(l)} + \lambda^{(l)})\frac{\partial^2 u^{(l)}}{\partial x \partial y} + (\lambda^{(l)} + 2\mu^{(l)})\frac{\partial^2 w^{(l)}}{\partial y^2}, \quad (x, y) \in \Omega^{(l)}. \tag{19b}$$

These equations are supplemented by boundary conditions on displacements and tractions (similar to those given in section 2.1) and detailed in Appendix B.

At the interface $y = 0$ we use the unit normal vector $\vec{n} = (n_1, n_2)$ pointing away from each subdomain as well as the unit tangent vector $\vec{m} = (n_2, -n_1)$, see Figure 2. The components of the traction vector at the interface are given by $T_i^{(l)} = \sigma_{ij}^{(l)} n_j^{(l)}$, for $l = 1, 2$; thus, the traction vectors on either side are

$$\vec{T}^{(1)} = (\sigma_{xy}^{(1)}, \sigma_{yy}^{(1)})$$

$$\vec{T}^{(2)} = (-\sigma_{xy}^{(2)}, -\sigma_{yy}^{(2)}).$$

Continuity conditions at the interface couple the two subdomains together. These involve jump conditions in displacements, and that the components of the traction vector be equal and opposite across the interface (i.e., $\sigma_{xy}^{(1)} = \sigma_{xy}^{(2)}$ and $\sigma_{yy}^{(1)} = \sigma_{yy}^{(2)}$). The interface conditions are thus given by

$$\text{(jump conditions)} \quad u^{(2)}(t,x,0) - u^{(1)}(t,x,0) = g_F(t,x), \tag{20a}$$

$$w^{(2)}(t,x,0) - w^{(1)}(t,x,0) = h_F(t,x), \tag{20b}$$

$$\text{(continuity conditions)} \quad \sigma_{xy}^{(1)}(t,x,0) - \sigma_{xy}^{(2)}(t,x,0) = 0, \tag{20c}$$

$$\sigma_{yy}^{(1)}(t,x,0) - \sigma_{yy}^{(2)}(t,x,0) = 0. \tag{20d}$$

In later sections the data g_F will be the slip we enforce, where slip is defined as the imposed value of the difference in the horizontal component of displacement across the interface. To show that (19) and (20) yield a well-posed problem can be done through the energy method as done in section 2.1 for the single domain. For two subdomains, the continuous energy for equation (19) is defined as the sum of the two contributions from each domain:

$$E = E^{(1)} + E^{(2)} \tag{21}$$

where

$$E^{(l)} = \int_{\Omega^{(l)}} \frac{\rho}{2}[(u_t^{(l)})^2 + (w_t^{(l)})^2] + \frac{1}{4\mu^{(l)}}\sigma_{ij}^{(l)}(\sigma_{ij}^{(l)} - \frac{\lambda^{(l)}}{3\lambda^{(l)} + 2\mu^{(l)}}\sigma_{kk}^{(l)}\delta_{ij})\, dx\, dy, \quad l = 1, 2. \tag{22}$$

Following a similar procedure as that done in section 2.1, we can show that

$$\dot{E} = 0, \tag{23}$$

see Appendix B for details. Estimate (23) is mimicked by the discrete equations, thus providing a stable discretization.

3.2. Semidiscrete Formulation and Energy Estimate

Following the analysis done in section 2.2, the semidiscretized governing equations in each domain are given by

$$\rho \mathbf{u}_{tt}^{(l)} = (\lambda^{(l)} + 2\mu^{(l)})[\mathbf{H}^{-1}(-\mathbf{A} + \mathbf{BS}) \otimes \mathbf{I}]\mathbf{u}^{(l)} + (\mu^{(l)} + \lambda^{(l)})(\mathbf{D} \otimes \mathbf{D})\mathbf{w}^{(l)} + \mu^{(l)}(\mathbf{I} \otimes \mathbf{H}^{-1}(-\mathbf{A} + \mathbf{BS}))\mathbf{u}^{(l)} + \mathbf{P}_1^{(l)} \tag{24a}$$

$$\rho \mathbf{w}_{tt}^{(l)} = \mu^{(l)}(\mathbf{H}^{-1}(-\mathbf{A} + \mathbf{BS}) \otimes \mathbf{I})\mathbf{w}^{(l)} + (\mu^{(l)} + \lambda^{(l)})(\mathbf{D} \otimes \mathbf{D})\mathbf{u}^{(l)} + (\lambda^{(l)} + 2\mu^{(l)})(\mathbf{I} \otimes \mathbf{H}^{-1}(-\mathbf{A} + \mathbf{BS}))\mathbf{w}^{(l)} + \mathbf{P}_2^{(l)}, \quad l = 1, 2. \tag{24b}$$

The SAT penalty vectors $\mathbf{P}_1^{(l)}$ and $\mathbf{P}_2^{(l)}$ in (24) depend on nine penalty parameters and impose the boundary conditions (given in Appendix B) and interface conditions (20) weakly, see Appendix B for details.

The semidiscrete energy is a sum of the energies from each subdomain, namely, $\mathbf{E} = \mathbf{E}^{(1)} + \mathbf{E}^{(2)}$ where

$$\mathbf{E}^{(l)} = \frac{\rho^{(l)}}{2}\left([\mathbf{u}_t^{(l)}]^T(\mathbf{H} \otimes \mathbf{H})\mathbf{u}_t^{(l)} + [\mathbf{w}_t^{(l)}]^T(\mathbf{H} \otimes \mathbf{H})\mathbf{w}_t^{(l)}\right) + \frac{1}{4\mu^{(l)}}[\sigma_{ij}^{(l)}]^T(\mathbf{H} \otimes \mathbf{H})(\sigma_{ij}^{(l)} - \frac{\lambda^{(l)}}{3\lambda^{(l)} + 2\mu^{(l)}}\sigma_{kk}^{(l)}\delta_{ij}) + \hat{\mathbf{d}}^{(l)}, \quad l = 1, 2. \tag{25}$$

The results for stable interface treatment from *Duru and Virta* [2014] show that the semidiscrete problem (24) exhibits an energy estimate such that

$$\dot{\mathbf{E}} \leq 0, \tag{26}$$

provided the penalty parameters are chosen properly, see Appendix B. Thus, (24) is a stable discretization of (19) and (20).

4. Frictional Interface Condition

The traction vectors on either side of the interface can be further decomposed into the normal component $\sigma^{(l)} = -\vec{n}^{(l)} \cdot \vec{T}^{(l)} = -\sigma_{yy}^{(l)}$ (taken to be positive in compression), and the shear component $\tau^{(l)} = \vec{m}^{(l)} \cdot \vec{T}^{(l)} = \sigma_{xy}^{(l)}$, for $l = 1, 2$, which must be continuous across the interface (see Figure 2). The fault interface is governed by rate-and-state friction that equates shear stress $\tau(x)$ on the fault with fault strength F

$$\tau = F(V, \psi), \tag{27}$$

where F is effective normal stress σ (normal stress minus pore pressure) on the fault times the friction coefficient f. The shear and effective normal stress used in the constitutive relation (27) requires use of the total values in stress, namely,

$$\tau = \tau^0 + \Delta\tau, \tag{28}$$

$$\sigma = \sigma^0 + \Delta\sigma, \tag{29}$$

where the background (or pre-) stresses τ^0, σ^0 are given functions along the interface and the stress changes $\Delta\tau, \Delta\sigma$ are obtained from solving the governing equations (24).

In the rate-and-state framework, the friction coefficient f is a function of slip velocity, which in this case is given by the time derivative of the change in the horizontal component of displacement on the fault

$$V(z, t) = \left.\frac{\partial u}{\partial t}\right|_{y=0^+} - \left.\frac{\partial u}{\partial t}\right|_{y=0^-} \tag{30}$$

and a state variable ψ in the following form

$$f(V, \psi) = a\sinh^{-1}\left(\frac{V}{2V_0}e^{\frac{\psi}{a}}\right) \tag{31}$$

[*Dieterich*, 1979; *Ruina*, 1983]. The state variable ψ undergoes its own time evolution given by

$$\frac{d\psi}{dt} = G(V, \psi). \tag{32}$$

While there are other forms for state-variable evolution, in this work we consider the classical aging law [*Marone*, 1998] where state can evolve in the absence of slip and may therefore be more appropriate for models accounting for the period of interseismic loading. The state variable evolution is given by

$$G(V, \psi) = -\frac{Vb}{D_c}\left(1 - e^{-\frac{f - f^{ss}(V)}{b}}\right), \tag{33}$$

where $f_{ss}(V) = f_0 - (b - a)\ln(V/V_0)$ is the steady state friction coefficient, f_0 is a reference friction coefficient for steady sliding at slip velocity V_0, a and b are dimensionless parameters characterizing the direct and state evolution effects, respectively, and D_c is the state evolution distance [*Marone*, 1998].

In our time-stepping procedure (detailed in the following section) we disregard inertia and thus solve the equations for static equilibrium (i.e., we set the left-hand side of (24) equal to 0). Since completely disregarding inertial effects can give rise to unbounded slip velocities [*Rice*, 1993], we use the radiation damping approximation to inertia. This comes from treating slip at each point as though it radiates as part of a plane (the extension of the local fault surface tangent) with uniform slip velocity and shear traction. For a bimaterial problem, the radiation damping stress is given by

$$\tau_{rad} = -\frac{\mu^{(1)}\mu^{(2)}}{c_s^{(1)}\mu^{(2)} + c_s^{(2)}\mu^{(1)}}V \tag{34}$$

which alters the constitutive relation (27) to

$$\tau - \eta V = F(V, \psi), \quad \text{where} \quad \eta = \frac{\mu^{(1)}\mu^{(2)}}{c_s^{(1)}\mu^{(2)} + c_s^{(2)}\mu^{(1)}}. \tag{35}$$

5. Time Stepping

In previous sections, we derive a provably stable discretization under the assumption of given boundary and interface data. Here we detail how the slip at the interface, g_F, is obtained by imposing the friction law (and depends on the solution at each time step).

In order to study earthquake cycles on a bimaterial fault, we load the system at the remote boundaries so that events nucleate spontaneously at the fault. The time-stepping method is detailed in *Erickson and Dunham* [2014] for the antiplane setting, but we summarize it here for the plane strain problem. We load the system at the top and bottom boundaries at a slow plate rate (denoted V_p) and assume periodic conditions the left and right boundaries (see Figure 2). The only nonzero boundary data are thus given by

$$g_B^{(1)} = -V_p t/2 \tag{36a}$$

$$g_T^{(2)} = V_p t/2. \tag{36b}$$

At the fault interface we impose jump conditions in displacements. The jump in horizontal displacement, or slip, is given by the data g_F which are obtained by integrating the slip velocity V (explained shortly). We also impose $h_F = 0$ so that the fault is restricted from opening. As done in *Erickson and Dunham* [2014], at each time step we solve the equations for static equilibrium given by

$$0 = (\lambda^{(l)} + 2\mu^{(l)})\frac{\partial^2 u^{(l)}}{\partial x^2} + (\mu^{(l)} + \lambda^{(l)})\frac{\partial^2 w^{(l)}}{\partial x \partial y} + \mu^{(l)}\frac{\partial^2 u^{(l)}}{\partial y^2} \tag{37a}$$

$$0 = \mu^{(l)}\frac{\partial^2 w^{(l)}}{\partial x^2} + (\mu^{(l)} + \lambda^{(l)})\frac{\partial^2 u^{(l)}}{\partial x \partial y} + (\lambda^{(l)} + 2\mu^{(l)})\frac{\partial^2 w^{(l)}}{\partial y^2}, \quad (x,y) \in \Omega^{(l)}, \tag{37b}$$

which are discretized using the right-hand side of (24). Time stepping is as follows:

1. Assume that at time t^n we know the slip $g_F^n = g_F(t^n, x)$ and the value of state $\psi^n = \psi(t^n, x)$.
2. Set $h_F^n = 0, g_B^{(1),n} = -V_p t^n/2, g_T^{(2),n} = V_p t^n/2$ and solve the quasi-static version of equation (24) to obtain the displacements $(\mathbf{u}^{(1),n}, \mathbf{w}^{(1),n})$ and $(\mathbf{u}^{(2),n}, \mathbf{w}^{(2),n})$ in the two sides of the domain. This involves solving one large linear system and makes up all of the computational work.
3. Use the displacements to compute the relevant components of stress in the domain:

$$\sigma_{xy}^{(1),n} = \mu^{(1)}(\mathbf{I} \otimes \mathbf{D})\mathbf{u}^{(1),n} + \mu^{(1)}(\mathbf{D} \otimes \mathbf{I})\mathbf{w}^{(1),n} \tag{38a}$$

$$\sigma_{yy}^{(1),n} = \lambda^{(1)}(\mathbf{D} \otimes \mathbf{I})\mathbf{u}^{(1),n} + (\lambda^{(1)} + 2\mu^{(1)})(\mathbf{I} \otimes \mathbf{D})\mathbf{w}^{(1),n} \tag{38b}$$

$$\sigma_{xy}^{(2),n} = \mu^{(2)}(\mathbf{I} \otimes \mathbf{D})\mathbf{u}^{(2),n} + \mu^{(2)}(\mathbf{D} \otimes \mathbf{I})\mathbf{w}^{(2),n} \tag{38c}$$

$$\sigma_{yy}^{(2),n} = \lambda^{(2)}(\mathbf{D} \otimes \mathbf{I})\mathbf{u}^{(2),n} + (\lambda^{(2)} + 2\mu^{(2)})(\mathbf{I} \otimes \mathbf{D})\mathbf{w}^{(2),n}. \tag{38d}$$

4. Evaluate the shear and normal stress components on the fault

$$\tau^{(1),n} = \left[\sigma_{xy}^{(1),n}\right]_T \tag{39a}$$

$$\sigma^{(1),n} = -\left[\sigma_{yy}^{(1),n}\right]_T \tag{39b}$$

$$\tau^{(2),n} = \left[\sigma_{xy}^{(2),n}\right]_B \tag{39c}$$

$$\sigma^{(2),n} = -\left[\sigma_{yy}^{(2),n}\right]_B. \tag{39d}$$

5. Compute the total stress values on the fault. In the continuous setting both the shear and normal stresses are continuous across the fault. However, since we enforce boundary conditions weakly, the two discrete solutions are equal up to the accuracy of the discretization. We take the stress change to be the average of the two:

$$\boldsymbol{\tau}^n = \boldsymbol{\tau}^0 + \Delta\boldsymbol{\tau}, \quad \text{where} \quad \Delta\boldsymbol{\tau} = (\boldsymbol{\tau}^{(1),n} + \boldsymbol{\tau}^{(2),n})/2 \tag{40a}$$

$$\boldsymbol{\sigma}^n = \boldsymbol{\sigma}^0 + \Delta\boldsymbol{\sigma}, \quad \text{where} \quad \Delta\boldsymbol{\sigma} = (\boldsymbol{\sigma}^{(1),n} + \boldsymbol{\sigma}^{(2),n})/2. \tag{40b}$$

6. Equate shear stress with frictional strength

$$\tau^n - \eta V^n = \sigma^n f(V^n, \psi^n) \tag{41}$$

and solve for the slip velocity V^n at time t^n. This requires a nonlinear solve on the fault for which we use a safe-guarded Newton iterative method.

7. Use the computed slip velocity V^n along with known state ψ^n to update both slip and state at the next time step (written in Forward Euler form here, but we use MATLAB's adaptive fourth-order ordinary differential equation solver ode45 with a relative tolerance of 10^{-7}):

$$g_F^{n+1} = g_F^n + \Delta t V^n \tag{42a}$$

$$\psi^{n+1} = \psi^n + \Delta t G(V^n, \psi^n) \tag{42b}$$

and return to step 2.

Note that in this work we solve the quasi-static equations and do not include a regularized normal stress response that has been used in dynamic simulations on bimaterial interfaces [*Ranjith and Rice*, 2001; *Ampuero and Ben-Zion*, 2008; *Shi and Day*, 2013] (see Appendix B for discussion).

6. Method Testing

To test the spatial accuracy of the discretization, we apply the method of manufactured solutions [*Roache*, 1998]. We construct an exact solution to the governing equations with modified boundary/interface conditions, adding source terms where necessary (i.e., where the manufactured solution fails to satisfy the governing equations). The solution is constructed so that it contains features we expect to see in our simulations. Specifically, we want the manufactured solution to be such that the fault remains locked during a long interseismic loading period after which abrupt sliding occurs during an event on much shorter time scales. The exact slip is given by

$$\delta(x) = \frac{A(t)}{2} d(x) + \frac{B(t)}{2} \left[2u_{max} - d(x) \right] \tag{43}$$

where the function

$$d(x) = \tanh\left[-(x - x_L) \right] + 1 + \tanh\left[x - x_R \right] + 1 \tag{44}$$

dictates the spatial dependency of motion on the fault and u_{max} is a parameter representing the maximum slip that occurs on the fault during rupture. $A(t) = V_p t$ will allow the outer sides of the fault to creep at a slow plate rate V_p during the interseismic period, and

$$B(t) = \frac{u_{max}}{2\pi} \left[\tan^{-1}\left(\frac{t - t_*}{t_w} \right) + \pi/2 \right] \tag{45}$$

is constructed so that the center region of the fault defined by the domain $x_L \leq x \leq x_R$ remains locked until an "event" occurs at time t_* (over a time scale t_w) and causes it to slide abruptly (slip velocities will range over 9 orders of magnitude). The remote boundaries will creep at the plate rate V_p. The exact solution is given by

$$u^{(1)}(t, x, y) = r^{(1)}(y)\frac{\delta(x)}{2} + s^{(1)}(y)\frac{V_p t}{2}, \tag{46a}$$

$$w^{(1)}(t, x, y) = a_0 \left[\sin(y) - y \right], \quad (x, y) \in [0, L_x] \times [-L_y/2, 0], \tag{46b}$$

Table 1. Parameters Used in the Manufactured Solution Convergence Tests

Parameter	Definition	Value
L_x	fault length	6π km
L_y	off-fault domain length	2π km
x_L	VS to VW transition	2π km
x_R	VW to VS transition	4π km
$\rho^{(1)}$	density on side 1	3333 kg/m^3
$\rho^{(2)}$	density on side 2	3333 kg/m^3
σ_n^0	background normal stress on fault	50 MPa
τ^0	background shear stress on fault	50 MPa
t_f	final simulation time	10^9 s
t_*	event nucleation time	$t_f/2$ s
a_0	amplitude of vertical displacement	0.1 m
t_w	timescale for event duration	10 s
u_{max}	maximum slip during event	1 m
a	rate-and-state parameter	0.015
b	rate-and-state parameter	0.02
D_c	critical slip distance	2 m
V_p	plate rate	10^{-9} m/s
V_0	reference velocity	10^{-6} m/s
f_0	reference friction coefficient	0.6
$\psi(0)$	initial state variable	$a\log[(2V_0/V(0))\sinh((\tau^0 - \eta V(0))/(\sigma_n a))]$

$$u^{(2)}(t,x,y) = r^{(2)}(y)\frac{\delta(x)}{2} + s^{(2)}(y)\frac{V_p t}{2}, \tag{46c}$$

$$w^{(2)}(t,x,y) = a_0\big(\lfloor\sin(y) - y\rfloor \quad (x,y) \in [0,L_x] \times [0,L_y/2], \tag{46d}$$

where a_0 is a model parameter that determines the amplitude of vertical displacement, and

$$r^{(1)}(y) = -(L_y/2 + y)/(L_y/2), \tag{47a}$$

$$r^{(2)}(y) = (L_y/2 - y)/(L_y/2), \tag{47b}$$

$$s^{(1)}(y) = y/(L_y/2), \tag{47c}$$

$$s^{(2)}(y) = y/(L_y/2) \tag{47d}$$

determine the y dependency of the manufactured solution off the fault. The interface lies at $y = 0$, and we assume bimaterial elastic moduli $\mu^{(1)} = 36$, $\mu^{(2)} = 20$, $v^{(1)} = v^{(2)} = 0.25$. All other parameters used are listed in Table 1, and the event occurs halfway through the simulated time interval. We use this manufactured solution to set all the boundary and interface data, as well as the source terms. To enforce the friction at the fault, we must also add a source term to the state evolution equation, as done in *Erickson and Dunham* [2014]. Figure 3a shows cumulative slip profiles along strike plotted in blue every 5 years during the interseismic period (defined to be when the maximum slip velocity along strike is less than 1 mm/s) and in dashed red every second during the quasi-dynamic event. Figure 3b shows the slip velocity at the center of the fault as a function of time (30 year simulation) time and corresponding zoom in Figure 3c where slip velocity increases over 9 orders of magnitude during the event which occurs at time t_*.

At the end of the simulation we compute the error made in both the discrete **H** and the energy norm. The discrete **H** norm is given by

$$||[\mathbf{u} \quad \mathbf{w}]^T||_{\mathbf{H}}^2 = \mathbf{u}^T(\mathbf{H} \otimes \mathbf{H})\mathbf{u} + \mathbf{w}^T(\mathbf{H} \otimes \mathbf{H})\mathbf{w} \tag{48}$$
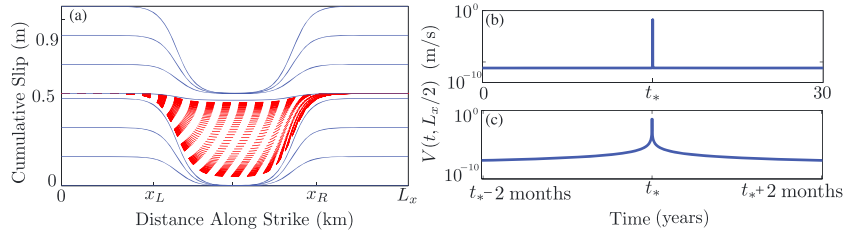
Figure 3. (a) Slip contours corresponding to the manufactured solution plotted in solid blue every 5 years during the interseismic period (max(V) < 1 mm/s) and in dashed red every second during quasi-dynamic rupture. (b) The 30 year time history and (c) zoom of slip velocity at the center point along strike. Fault remains locked with slip velocity ~10^{-9} m/s until an event occurs at time t_* during which slip velocity increases over 9 orders of magnitude.

and the discrete energy norm is given by (we ignore kinetic energy since we are solving the quasi-static equations)

$$||[\mathbf{u} \quad \mathbf{w}]^T||_{\mathbf{E}}^2 = \frac{1}{4\mu}\sigma_{ij}^T(\mathbf{H} \otimes \mathbf{H})(\sigma_{ij} - \frac{\lambda}{3\lambda + 2\mu}\sigma_{kk}\delta_{ij}) + \hat{\mathbf{d}}. \tag{49}$$

Thus, the errors are given by

$$\text{Error}_H(h) = \sum_{l=1,2} ||[\mathbf{u}^{(l)} - \hat{\mathbf{u}}^{(l)} \quad \mathbf{w}^{(l)} - \hat{\mathbf{w}}^{(l)}]^T||_{\mathbf{H}} \tag{50}$$

$$\text{Error}_E(h) = \sum_{l=1,2} ||[\mathbf{u}^{(l)} - \hat{\mathbf{u}}^{(l)} \quad \mathbf{w}^{(l)} - \hat{\mathbf{w}}^{(l)}]^T||_{\mathbf{E}}, \tag{51}$$

where the hat vectors $\hat{\mathbf{u}}$ and $\hat{\mathbf{w}}$ are the exact solutions evaluated at the grid points. The results for the second-order accurate operators are listed in Table 2 which shows that our method is converging to the true solution at the expected rate.

7. Application

We are interested in the effect of material mismatch across the fault interface over the earthquake cycle. Keeping the material density ρ and Poisson's ratio ν constant, we vary the shear modulus μ on either side of the fault. Although ρ does not explicitly appear in the discretized equilibrium equations (24), it does enter at the fault interface through the radiation damping stress (35). We vary the frictional parameters a and b along strike which introduces the length scale L_v of the velocity-weakening (seismogenic) zone, see Figure 4. This velocity-weakening zone transitions to a region of velocity-strengthening zones on either end of the fault. The friction law introduces the critical nucleation length scale

$$h^* = \pi\frac{\mu^* D_c}{(b-a)\sigma}, \tag{52}$$

where $\mu^* = \mu/(1-\nu)$ for mode II rupture [*Rice and Ruina*, 1983; *Rice*, 1993; *Rubin and Ampuero*, 2005], which must be resolved to ensure accuracy of the solution [*Rice*, 1993]. There is also another length scale to be resolved which is the region of rapid strength degradation immediately behind the rupture tip (usually much smaller than h^*) which, for the aging law is

$$L_b = \mu^* D_c/(\sigma b) \tag{53}$$

[*Rubin and Ampuero*, 2005].

Table 2. Error in the Discrete **H** and Energy Norms With $N = N_x = 2N_y$[a]

N	$\text{Error}_H(h)$	Rate	$\text{Error}_E(h)$	Rate
2^4	8.734×10^{-1}	—	1.195×10^0	–
2^5	1.533×10^{-1}	2.510	2.465×10^{-1}	2.278
2^6	3.868×10^{-2}	1.987	6.103×10^{-2}	2.014
2^7	9.683×10^{-3}	1.998	1.520×10^{-2}	2.005
2^8	2.419×10^{-3}	2.001	3.795×10^{-3}	2.002

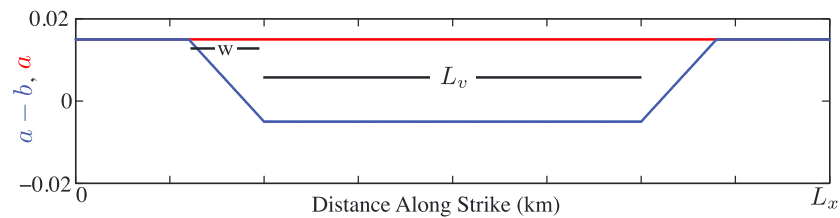[a]The rate of convergence approaches 2, as expected for a method with second-order accuracy.

Figure 4. Frictional parameter *a* (red) is held constant, while *b* varies along strike. Two velocity-strengthening zones ($a - b > 0$) surround a velocity-weakening zone ($a - b < 0$) of length L_v and transition width w.

For the monomaterial case, the effective normal stress remains constant in time $\sigma = \sigma^{(0)}$, and thus, we can calculate the length scales h^* and L_b directly. Bimaterial properties, however, generate perturbations in normal stress, which makes these length scales more difficult to compute. In previous analytical and numerical studies of fully dynamic rupture problems, normal stress changes can be quite large, increase with rupture speed and/or propagation distance, and can lead to fault opening [*Adams*, 1995; *Andrews and Ben-Zion*, 1997; *Ben-Zion and Huang*, 2002; *Dalguer and Day*, 2009]. In our quasi-dynamic simulations, however, we find that $\Delta\sigma$ is only a small fraction of $\sigma^{(0)}$. That only small changes in normal stress occur in our simulations is likely due in part to the radiation damping approximation to inertia which tends to produce slower rupture speeds than fully dynamic simulations [*Lapusta and Liu*, 2009; *Thomas et al.*, 2014]. Our simulations allow rupture to propagate at most 30 km or so and might generate higher amplitude normal stress changes if this length scale were increased. For now, however, we approximate h^* and L_b using $\sigma = \sigma^{(0)}$. In all our simulations we resolve L_b with at least three grid points (corresponding to $h^*/\Delta x \approx 13$), which is on the lower end of grid resolution compared with the simulations of *Lapusta et al.* [2000] but appears adequate (Appendix C shows that simulations with higher resolution yield virtually identical results). All other parameter values we consider for the application simulations are listed in Table 3.

For the monomaterial case, the problem is symmetric about the center point of the fault $x = L_x/2$, but we found that our simulations lose symmetry with increasing simulation time due to round off error (a feature seen elsewhere in *Ampuero and Rubin* [2008]). Figure 5 shows slip contours for the monomaterial case with $D_c = 16$ mm. The slip profiles are plotted in solid blue contours every 5 years during the interseismic period

Table 3. Parameters Used in the Earthquake Cycle Simulations

| Parameter	Definition	Value
L_x	fault length	60 km
L_y	off-fault domain length	60 km
L_v	VW patch length	40 km
w	VS to VS transition length scale	4 km
$\mu^{(1)}$	shear modulus on side 1	30 GPa
$\mu^{(2)}$	shear modulus on side 2	variable GPa
$\rho^{(1)}$	density on side 1	3333 kg/m^3
$\rho^{(2)}$	density on side 2	3333 kg/m^3
$\nu^{(1)}$	Poisson's ratio on side 1	0.25
$\nu^{(2)}$	Poisson's ratio on side 2	0.25
σ^0	background normal stress on fault	50 MPa
τ^0	background shear stress on fault	0 MPa
a	rate-and-state parameter	0.015
b	rate-and-state parameter	variable along strike
D_c	critical slip distance	variable mm
V_p	plate rate	10^{-9} m/s
V_0	reference velocity	10^{-6} m/s
f_0	reference friction coefficient	0.6
$\psi(0)$	initial state variable	0.6
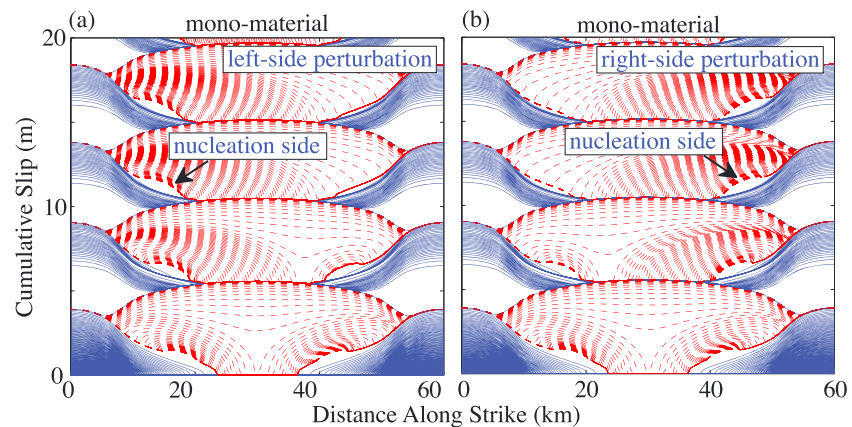
Figure 5. Cumulative slip profiles plotted in solid blue contours every 5-a during the interseismic period (max(V) < 1 mm/s) and in dashed red contours every second during quasi-dynamic rupture for the monomaterial problem with $D_c = 16$ mm. The originally symmetric problem is perturbed by adding a small value of 10^{-6} to the initial value of the state variable (initially constant) at (a) $x = 10$ km and (b) $x = 50$ km.

(when the maximum value of slip velocity V along the fault is less than 1 mm/s) and in dashed red every second during quasi-dynamic rupture. Figure 5a shows results from adding a small perturbation of 10^{-6} to the initial value of the state variable (initially constant) at a single point on the left side of the fault (at $x = 10$ km). Initially, two events nucleate on either end of the fault and meet in the middle, but this symmetry is lost by the third event which nucleates on the left side and propagates right for the rest of the cycle. This direction can be switched by adding the perturbation near the right side of the fault, as done in Figure 5b. Figure 6 is the analogous study when halving D_c to 8 mm. Both small and large events emerge (seen elsewhere [*Lapusta and Rice*, 2003]), but the problem also loses symmetry. The first large, asymmetric event nucleates on either the left or right side, depending on the perturbation, and subsequent events alternate sides. The monomaterial problem is therefore unstable to small perturbations.

Figures 7 and 8 are similar perturbation studies for the problem with a 5% material contrast. $\mu^{(1)}$ is fixed at 30 GPa and $\mu^{(2)}$ is reduced to ≈ 28.6 GPa. Given the loading conditions (see Figure 2), the preferred rupture direction is to the right (particle motion of the side of the fault with lower shear wave velocity). Figure 7 shows that the bimaterial problem with $D_c = 16$ mm is stable to the initial perturbation, and all events propagate in the preferred direction. Figure 8 shows results when $D_c = 8$ mm. All large events propagate in the preferred direction, but occasional small events propagate in the nonpreferred direction. This behavior is stable to perturbations as well, which assures us that results from our bimaterial simulations contain robust features.
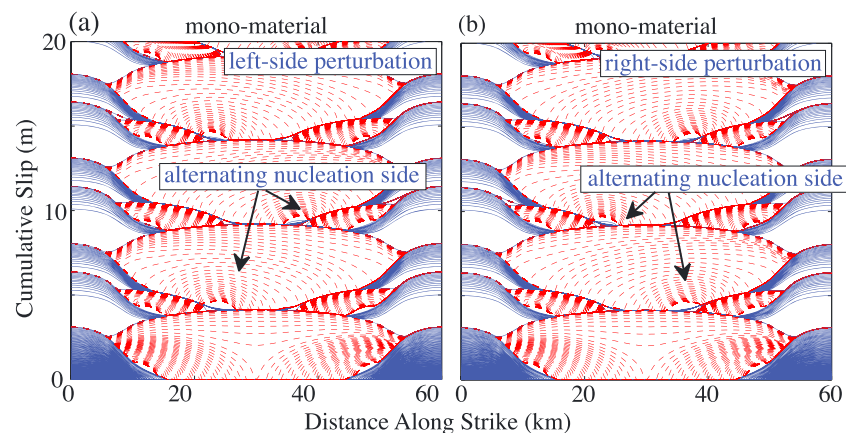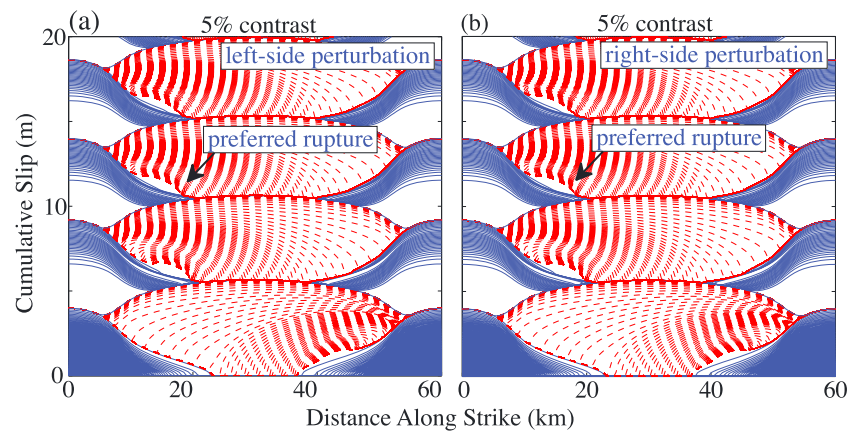

Figure 6. Cumulative slip profiles plotted in solid blue contours every 5-a during the interseismic period (max(V) < 1 mm/s) and in dashed red contours every second during quasi-dynamic rupture for the monomaterial problem with $D_c = 8$ mm. The originally symmetric problem is perturbed by adding a small value of 10^{-6} to the initial value of the state variable (initially constant) at (a) $x = 10$ km and (b) $x = 50$ km.

Figure 7. Cumulative slip profiles plotted in solid blue contours every 5-a during the interseismic period (max(V) < 1 mm/s) and in dashed red contours every second during quasi-dynamic rupture for the bimaterial problem (5% contrast) with $D_c = 16$ mm. The problem is perturbed by adding a small value of 10^{-6} to the initial value of the state variable (initially constant) at (a) $x = 10$ km and (b) $x = 50$ km.

We further consider a 10 and 20% contrast (i.e., $\mu^{(2)} \approx 27.3$ and $\mu^{(2)} \approx 25$ GPa, respectively). For $D_c = 16$ mm (see Figure 9), all ruptures nucleate on the left-hand side and propagate to the right so that rupture is predominantly in the preferred direction (as seen in the 5% contrast in Figure 7). The simulations with higher contrasts reveal that increasing material mismatch causes slightly more slip to accumulate during each event (and thus a slightly longer recurrence interval between events).

Figure 10 shows results for $D_c = 8$ mm. Similar to the results with a 5% contrast in Figure 8, a 10 and 20% show that a small event nucleates on the left-hand side (near the transition zone) and propagates predominantly to the right (in the preferred direction) before terminating. A few years later, a second small event nucleates at the right transition zone and propagates in the nonpreferred direction. These are then followed by a large event that nucleates where the first small event terminated (to the left of the center of the fault, around 20 km along strike) and propagates predominantly in the preferred direction.

Figure 11 shows the recurrence interval for the simulations in Figures 5–10. Figure 11a shows maximum slip velocity on the fault for $D_c = 16$ mm where only large events emerge (rupturing the full extent of fault). The recurrence interval is approximately 146 years for the monomaterial case (black), 152 years for a 5% contrast (blue), 154 years for a 10% contrast (red), and 156 years for the 20% contrast (cyan). Figure 11b shows maximum slip velocity on the fault for $D_c = 8$ mm where all simulations involve large and small events. For
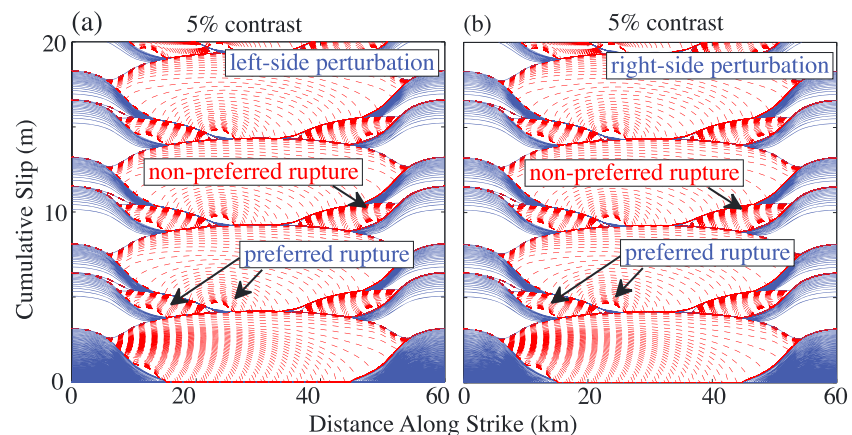

Figure 8. Cumulative slip profiles plotted in solid blue contours every 5-a during the interseismic period (max(V) < 1 mm/s) and in dashed red contours every second during quasi-dynamic rupture for the bimaterial problem (5% contrast) with $D_c = 8$ mm. The problem is perturbed by adding a small value of 10^{-6} to the initial value of the state variable (initially constant) at (a) $x = 10$ km and (b) $x = 50$ km.
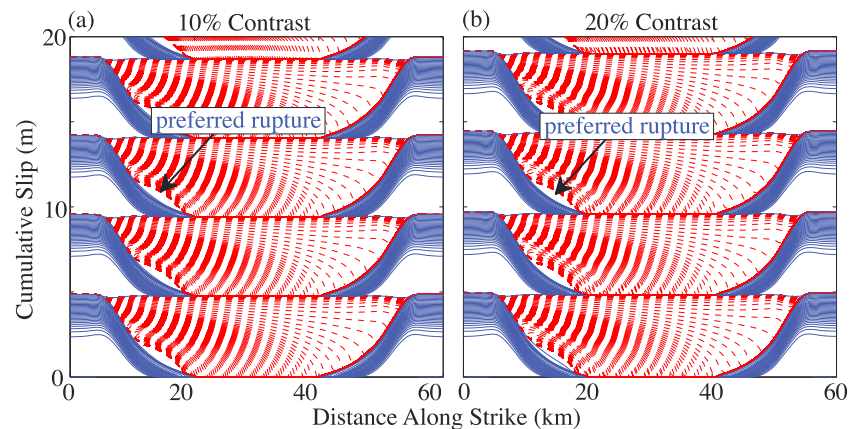
Figure 9. Cumulative slip profiles plotted in solid blue contours every 5-a during the interseismic period (max(V) < 1 mm/s) and in dashed red contours every second during quasi-dynamic rupture for a (a) 10% and (b) 20% contrast with D_c = 16 mm.

the monomaterial case (black) the recurrence interval for the large event is approximately 161 years, with the smaller event nucleating approximately 69 years after the large events (see zoom in Figure 11). For the 5% contrast (blue) the recurrence interval of the single large event propagating in the preferred direction is approximately 164 years, with two smaller events nucleating at 69 and 69.5 years after the large event. For the 10% contrast (red) the recurrence interval for the large rupture in the preferred direction is 168 years, with small events occur approximately 68.5 and 70 years after the large event. For the 20% contrast (cyan) the recurrence interval for the large, preferred rupture is 178 years, with small events occurring approximately 67.5 and 69.5 years after the large event. Material contrast does increase the recurrence interval for large events in all of these simulations, and more so for the case of smaller D_c, but this effect is most likely augmented by the fact that the smaller events relieve some of the accumulated stress on the fault. Furthermore, increasing material mismatch allows the first small event to nucleate sooner, most likely due to a decreased critical nucleation length h^*.

In order to understand rupture directivity in these simulations, Figure 12 shows the slip velocity (blue) and normal stress change (green) for the results in Figure 10a, plotted every 5 s during the first small event (time represented by fading colors). The normal stress change immediately behind the rupture tip is tensile in the preferred direction and compressional in the nonpreferred direction, in agreement with theoretical predictions, and rupture propagates like an asymmetric, bilateral crack.
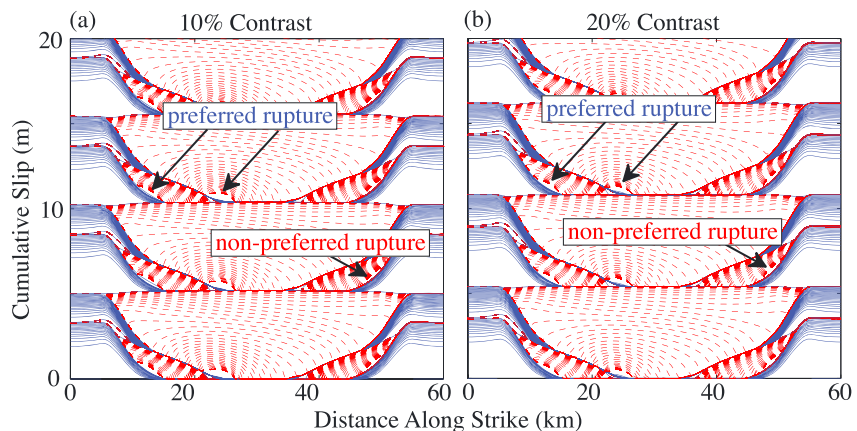

Figure 10. Cumulative slip profiles plotted in solid blue contours every 5-a during the interseismic period (max(V) < 1 mm/s) and in dashed red contours every second during quasi-dynamic rupture for a (a) 10% and (b) 20% contrast with D_c = 8 mm.
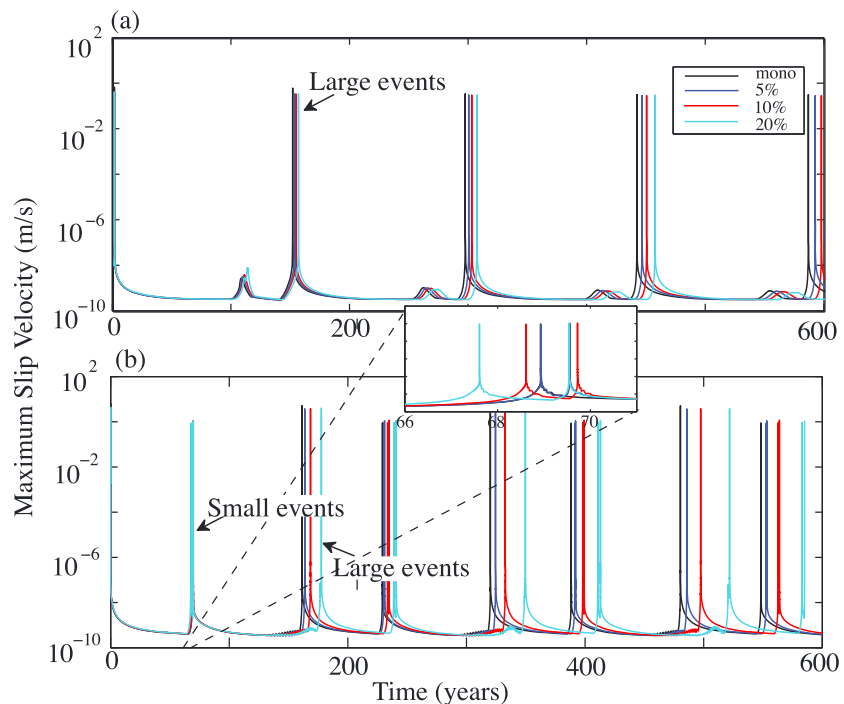
Figure 11. The 600 year time histories of maximum slip velocity for (a) $D_c = 16$ mm and (b) $D_c = 8$ mm (with corresponding zoom over time period 66 to 71 years). Contrasts in shear modulus are given for the monomaterial case (black), 5% contrast (blue), 10% contrast (red), and 20% contrast (cyan). For $D_c = 16$ mm, only large events emerge (events rupturing entire length of the fault),with recurrence intervals that increase with increasing material mismatch. For $D_c = 8$ mm, both large and small events emerge.

Figure 13 shows slip velocity and shear to normal stress ratio for the results in Figure 10a over about a 160 year period. This simulation is characterized by a first small event that nucleates on the left at a time we denote t_0. Sixty years prior to this event, the shear to normal stress ratio appears symmetric about the center of the fault ($L_x = 30$ km), as shown in Figure 13a. The bimaterial effect, however, introduces an asymmetry such that the shear to normal stress ratio is slightly higher on the left side of the fault (see Figure 13b); thus, the first small event nucleates on the left and propagates with a higher slip velocity and faster rupture speed to the right (the preferred direction, see Figures 13c–13e). This small event reduces the stress on the left side (see Figure 13f), while the right side is primed for rupture. A short (≈ 1 year) quasi-static loading period ensues and rupture nucleates on the right at time t_1, propagating predominantly in the nonpreferred direction, see Figures 13g and 13h. After these two small events, the shear to normal stress ratio appears fairly symmetric, see Figure 13i. An approximate 100 year loading period ensues and nucleation is again favored to the left of the center of the fault, where the first small event terminated, see Figures 13j–13l. After this large event, the cycle repeats.
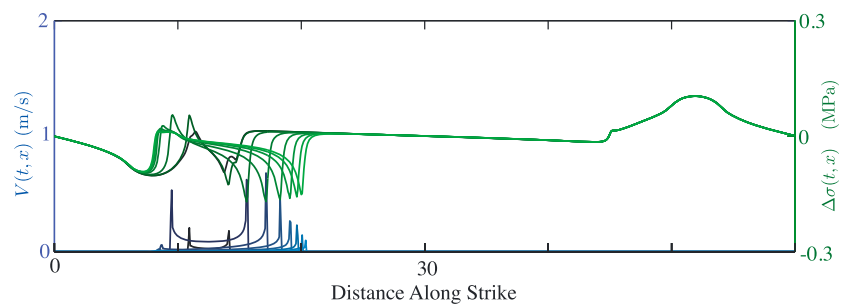

Figure 12. Slip velocity (blue) and normal stress perturbation (green) for the simulation in Figure 10a plotted every 5 s during the first small event (time shown in fading colors). The stress perturbation in the region behind the rupture tip is tensile in the preferred direction (to the right) and compressional in the nonpreferred direction.
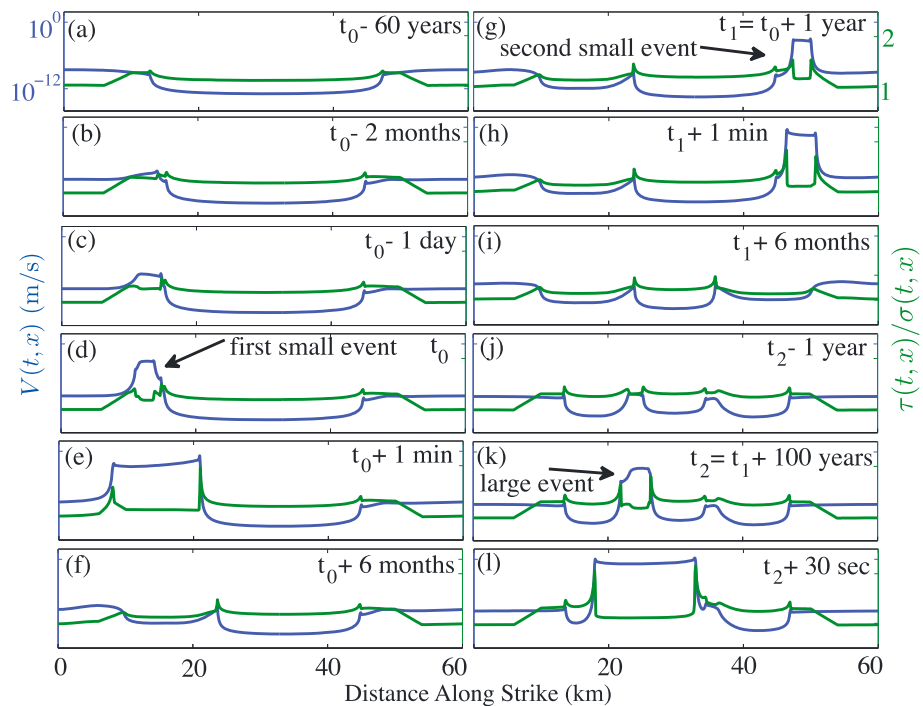
Figure 13. Slip velocity (blue) and shear to normal stress ratio (green) for the simulation in Figure 10a over an approximate 160 year period. Time t_0 corresponds to nucleation of the first small event on the left side of the fault. (a) Sixty years, (b) 2 months, and (c) 1 day prior to nucleation of the first small event at (d) time t_0. (e) One minute and (f) 6 months after the first event. (g) The second small event nucleates on the right at time t_1, about 1 year after t_0. (h) One min and (i) 6 months after second small event. (j) One year prior to the large event that nucleates (k) at time t_2 to the left of the center of the fault approximately 100 years after the second small event. (l) Thirty seconds after the large event nucleates.

8. Discussion

In this work we consider a planar fault where a velocity weakening patch is surrounded by two velocity-strengthening patches, and all events nucleate near one of the two transitions zones. Our results suggest that if initial conditions on the fault are symmetric (about the center of the fault), then bimaterial properties introduce heterogeneous (asymmetric) stress conditions along the fault, giving rise to a preferred nucleation site. This favored nucleation site is at the left transition zone where rupture propagates predominantly into the velocity-weakening patch and thus in the preferred direction. The right nucleation site, however, is less likely to host rupture in the preferred direction because rupture has to propagate into a velocity-strengthening zone. Rupture in the preferred direction is thus correlated with a preferred nucleation site. The resulting rupture behaviors align with the laboratory studies of *Anooshehpoor and Brune* [1999] that show clear tendency for preferred propagation direction despite the existence of stress heterogeneities. For smaller values of D_c, however, small events relieve stress on parts of the fault and allow nonpreferred rupture to take place. By decreasing D_c, smaller events are likely to emerge, and conditions may exist under which large ruptures propagating in the nonpreferred direction are possible, or that a larger fraction of ruptures may propagate in the nonpreferred direction.

Possible rupture in the nonpreferred direction could be further explored by incorporating other sources of heterogeneity (a heterogeneous distribution of frictional parameters a and b, for example) and exploring if heterogeneity dominates bimaterial effects as seen in *Andrews and Harris* [2005]. The 3-D effects may also increase the tendency for preferred rupture direction of large events [*Dalguer and Day*, 2009; *Brietzke et al.*, 2009]. Rupture directivity in nature is probably further influenced by fault geometry and off-fault plastic response, which, over the long-term cycle would evolve a heterogeneous stress field that might also favor rupture to occur in the nonpreferred direction. An earthquake cycle model with these features will be the next step in our work along with the comparison of the results from our model to the observational statistics of earthquake directivity.

All of our simulations were done with the aging law for state evolution, and we observed asymmetric, crack-like bilateral rupture. In future work we plan to study the interplay between stress heterogeneities and bimaterial effects with a friction law with a strong rate-weakening response, which may enhance the tendency for preferred propagation direction of large events as seen in *Ampuero and Ben-Zion* [2008]. In addition, it will be interesting to determine whether the slip law form for state evolution (with strong rate weakening) allows for pulse-like rupture or if unilateral rupture is possible. For the parameters we consider, we observed only small changes in normal stress during rupture, which we believe is due to several contributing factors including the radiation damping approximation to inertia and limited rupture speed and propagation distance. Future work will consider decreased values of D_c (which influences resulting rupture speeds) and greater fault lengths, in order to determine if larger amplitude normal stress changes occur and how they influence rupture.

The model setup for the simulations in section 7 are affected by the highest strain rate present in the problem. For the simulations in this work, the off-fault distance L_y defines a parameter of the problem, i.e., the strain rate V_p/L_y. We thus consider a strain rate of approximately 10^{-6}/year, which is not unreasonable given measured values at the San Andreas Fault [*Fialko*, 2006; *Chéry*, 2008]. Ideally, we would like our results to be independent of the off-fault distance, which could be done by taking $L_y \gg L_v$ and ensuring that L_x is large enough so that the velocity-strengthening regions on either end of the fault creep at the plate rate V_p. This ideal setup will be something we explore in future work with a parallelized code.

Appendix A: Penalty Terms for Section 2

At the left and right boundaries we introduce the following notation for obtaining the traction components, namely,

$$\mathbf{T}_x = (\lambda + 2\mu)(\mathbf{S} \otimes \mathbf{I})\mathbf{u} + \lambda(\mathbf{I} \otimes \mathbf{D})\mathbf{w} \tag{A1}$$

$$\mathbf{T}_y = \mu[(\mathbf{I} \otimes \mathbf{D})\mathbf{u} + (\mathbf{S} \otimes \mathbf{I})\mathbf{w}]. \tag{A2}$$

Recall that $\mathbf{S}$ approximates the first derivative at the boundary. Therefore, in equation (A2), $\mathbf{S} \otimes \mathbf{I}$ can be used to approximate the derivative $\partial/\partial x$ at the left and right boundaries, but $\mathbf{I} \otimes \mathbf{D}$ must be used to approximate $\partial/\partial y$.

We introduce the notation $\mathbf{u}_B$, for example, to denote the grid vector approximating u at the bottom boundary ($y = -L_y/2$) and use subscripts $T, L,$ and R similarly to denote the grid vectors at the top, left, and right boundaries, respectively. The discrete version of the boundary conditions (4) are thus

$$\mathbf{u}_B = \mathbf{g}_B, \quad \mathbf{w}_B = \mathbf{h}_B, \tag{A3}$$

$$\mathbf{u}_T = \mathbf{g}_T, \quad \mathbf{w}_T = \mathbf{h}_T, \tag{A4}$$

$$\mathbf{u}_R - \mathbf{u}_L = 0, \tag{A5}$$

$$\mathbf{w}_R - \mathbf{w}_L = 0, \tag{A6}$$

$$[\mathbf{T}_x]_R - [\mathbf{T}_x]_L = 0, \tag{A7}$$

$$[\mathbf{T}_x]_R - [\mathbf{T}_x]_L = 0, \tag{A8}$$

where $\mathbf{g}_B = g_B(x_j), j = 0, \dots N_x$, is the boundary data evaluated at the grid points, and $\mathbf{g}_T, \mathbf{h}_B, \mathbf{h}_T$ are defined similarly.

The damping term $\hat{\mathbf{d}}$ is given by

$$\hat{\mathbf{d}} = \frac{1}{2}\left[(\lambda + 2\mu)\mathbf{u}^T(\mathbf{R} \otimes \mathbf{H})\mathbf{u} + \mu\mathbf{u}^T(\mathbf{H} \otimes \mathbf{R})\mathbf{u} + \mu\mathbf{w}^T(\mathbf{R} \otimes \mathbf{H})\mathbf{w} + (\lambda + 2\mu)\mathbf{w}^T(\mathbf{H} \otimes \mathbf{R})\mathbf{w}\right],$$

and the time derivative of (17) is

$$\dot{\mathbf{E}} := \frac{\rho}{2}\left(\mathbf{u}_{tt}^T(\mathbf{H}\otimes\mathbf{H})\mathbf{u}_t + \mathbf{u}_t^T(\mathbf{H}\otimes\mathbf{H})\mathbf{u}_{tt} + \mathbf{w}_{tt}^T(\mathbf{H}\otimes\mathbf{H})\mathbf{w}_t + \mathbf{w}_t^T(\mathbf{H}\otimes\mathbf{H})\mathbf{w}_{tt}\right)$$
$$+ \frac{d}{dt}\left[\frac{1}{4\mu}\sigma_{ij}^T(\mathbf{H}\otimes\mathbf{H})\left(\sigma_{ij} - \frac{\lambda}{3\lambda+2\mu}\sigma_{kk}\delta_{ij}\right) + \hat{\mathbf{d}}\right]. \tag{A9}$$

Using the superscripts d_1 and d_2 to denote enforcement of boundary conditions on displacements and s_1, s_2 to denote those on tractions (stresses), respectively, the penalty vectors in (15) that enforce boundary conditions weakly are given by

$$\mathbf{P}_1 = \mathbf{p}_B^{d_1} + \mathbf{p}_T^{d_1} + \mathbf{p}_L^{d_1} + \mathbf{p}_R^{d_1} + \mathbf{p}_L^{s_1} + \mathbf{p}_R^{s_1} \tag{A10}$$

$$\mathbf{P}_2 = \mathbf{p}_B^{d_2} + \mathbf{p}_T^{d_2} + \mathbf{p}_L^{d_2} + \mathbf{p}_R^{d_2} + \mathbf{p}_L^{s_2} + \mathbf{p}_R^{s_2} \tag{A11}$$

where

$$\mathbf{p}_B^{d_1} = \alpha_B(\mathbf{I}\otimes\mathbf{H}^{-1})\tilde{\mathbf{E}}_B(\mathbf{u}_B - \mathbf{g}_B) - \beta(\mathbf{I}\otimes\mathbf{H}^{-1})[\mu(\mathbf{I}\otimes\mathbf{S}^T)]\tilde{\mathbf{E}}_B(\mathbf{u}_B - \mathbf{g}_B) - \beta(\mathbf{I}\otimes\mathbf{H}^{-1})[\lambda(\mathbf{D}^T\otimes\mathbf{I})]\tilde{\mathbf{E}}_B(\mathbf{w}_B - \mathbf{h}_B), \tag{A12}$$

$$\mathbf{p}_T^{d_1} = \alpha_T(\mathbf{I}\otimes\mathbf{H}^{-1})\tilde{\mathbf{E}}_T(\mathbf{u}_T - \mathbf{g}_T) + \beta(\mathbf{I}\otimes\mathbf{H}^{-1})[\mu(\mathbf{I}\otimes\mathbf{S}^T)]\mathbf{E}_T(\mathbf{u}_T - \mathbf{g}_T) + \beta(\mathbf{I}\otimes\mathbf{H}^{-1})[\lambda(\mathbf{D}^T\otimes\mathbf{I})]\tilde{\mathbf{E}}_T(\mathbf{w}_T - \mathbf{h}_T), \tag{A13}$$

$$\mathbf{p}_L^{d_1} = -\alpha_L(\mathbf{H}^{-1}\otimes\mathbf{I})\tilde{\mathbf{E}}_L(-\mathbf{u}_R+\mathbf{u}_L) + \beta_L(\mathbf{H}^{-1}\otimes\mathbf{I})\left[c(\mathbf{S}^T\otimes\mathbf{I})\right]\mathbf{E}_L(\mathbf{u}_R-\mathbf{u}_L) + \beta_L(\mathbf{H}^{-1}\otimes\mathbf{I})\left[\mu(\mathbf{I}\otimes\mathbf{D}^T)\right]\mathbf{E}_L(\mathbf{w}_R-\mathbf{w}_L), \tag{A14}$$

$$\mathbf{p}_R^{d_1} = -\alpha_R(\mathbf{H}^{-1}\otimes\mathbf{I})\tilde{\mathbf{E}}_R(\mathbf{u}_R-\mathbf{u}_L) + \beta_R(\mathbf{H}^{-1}\otimes\mathbf{I})\left[c(\mathbf{S}^T\otimes\mathbf{I})\right]\tilde{\mathbf{E}}_R(\mathbf{u}_R-\mathbf{u}_L) + \beta_R(\mathbf{H}^{-1}\otimes\mathbf{I})\left[\mu(\mathbf{I}\otimes\mathbf{D}^T)\right]\tilde{\mathbf{E}}_R(\mathbf{w}_R-\mathbf{w}_L), \tag{A15}$$

$$\mathbf{p}_L^{s_1} = -\epsilon(\mathbf{H}^{-1}\otimes\mathbf{I})\tilde{\mathbf{E}}_L\left([\mathbf{T}_x]_R - [\mathbf{T}_x]_L\right), \tag{A16}$$

$$\mathbf{p}_R^{s_1} = -\epsilon(\mathbf{H}^{-1}\otimes\mathbf{I})\tilde{\mathbf{E}}_R\left([\mathbf{T}_x]_R - [\mathbf{T}_x]_L\right) \tag{A17}$$

and

$$\mathbf{p}_B^{d_2} = \alpha_B(\mathbf{I}\otimes\mathbf{H}^{-1})\tilde{\mathbf{E}}_B(\mathbf{w}_B-\mathbf{h}_B) - \beta(\mathbf{I}\otimes\mathbf{H}^{-1})[(\lambda+2\mu)(\mathbf{I}\otimes\mathbf{S}^T)]\tilde{\mathbf{E}}_B(\mathbf{w}_B-\mathbf{h}_B) - \beta(\mathbf{I}\otimes\mathbf{H}^{-1})[\mu(\mathbf{D}^T\otimes\mathbf{I})]\tilde{\mathbf{E}}_B(\mathbf{u}_B-\mathbf{g}_B), \tag{A18}$$

$$\mathbf{p}_T^{d_2} = \alpha_T(\mathbf{I}\otimes\mathbf{H}^{-1})\tilde{\mathbf{E}}_T(\mathbf{w}_T-\mathbf{h}_T) + \beta(\mathbf{I}\otimes\mathbf{H}^{-1})[(\lambda+2\mu)(\mathbf{I}\otimes\mathbf{S}^T)]\tilde{\mathbf{E}}_T(\mathbf{w}_T-\mathbf{h}_T) + \beta(\mathbf{I}\otimes\mathbf{H}^{-1})[\mu(\mathbf{D}^T\otimes\mathbf{I})]\tilde{\mathbf{E}}_T(\mathbf{u}_T-\mathbf{g}_T), \tag{A19}$$

$$\mathbf{p}_L^{d_2} = -\alpha_L(\mathbf{H}^{-1}\otimes\mathbf{I})\tilde{\mathbf{E}}_L(-\mathbf{w}_R+\mathbf{w}_L) + \beta_L(\mathbf{H}^{-1}\otimes\mathbf{I})\left[\mu(\mathbf{S}^T\otimes\mathbf{I})\right]\tilde{\mathbf{E}}_L(\mathbf{w}_R-\mathbf{w}_L) + +\beta_L(\mathbf{H}^{-1}\otimes\mathbf{I})\left[\lambda(\mathbf{I}\otimes\mathbf{D}^T)\right]\tilde{\mathbf{E}}_L(\mathbf{u}_R-\mathbf{u}_L), \tag{A20}$$

$$\mathbf{p}_R^{d_2} = -\alpha_R(\mathbf{H}^{-1}\otimes\mathbf{I})\tilde{\mathbf{E}}_R(\mathbf{w}_R-\mathbf{w}_L) + \beta_R(\mathbf{H}^{-1}\otimes\mathbf{I})\left[\mu(\mathbf{S}^T\otimes\mathbf{I})\right]\tilde{\mathbf{E}}_R(\mathbf{w}_R-\mathbf{w}_L) + \beta_R(\mathbf{H}^{-1}\otimes\mathbf{I})\left[\lambda(\mathbf{I}\otimes\mathbf{D}^T)\right]\tilde{\mathbf{E}}_R(\mathbf{u}_R-\mathbf{u}_L), \tag{A21}$$

$$\mathbf{p}_L^{s_2} = -\epsilon(\mathbf{H}^{-1}\otimes\mathbf{I})\tilde{\mathbf{E}}_L\left([\mathbf{T}_y]_R - [\mathbf{T}_y]_L\right), \tag{A22}$$

$$\mathbf{p}_R^{s_2} = -\epsilon(\mathbf{H}^{-1}\otimes\mathbf{I})\tilde{\mathbf{E}}_R\left([\mathbf{T}_y]_R - [\mathbf{T}_y]_L\right), \tag{A23}$$

where matrices $\tilde{\mathbf{E}}_B, \tilde{\mathbf{E}}_T, \tilde{\mathbf{E}}_L$, and $\tilde{\mathbf{E}}_R$ map the numerical solutions at the boundaries to full-length vectors, and $\alpha_B, \alpha_T, \alpha_L, \alpha_R, \beta, \beta_L, \beta_R$, and ϵ are six penalty parameters whose values are chosen in order to obtain a stable discretization. *Duru and Virta* [2014] show that if the penalty parameters satisfy

$$\alpha_B, \alpha_T \leq -\max\left(\frac{4\mu}{4\gamma\Delta y}, \frac{4(\lambda + 2\mu)}{4\gamma\Delta y}\right), \quad \beta = 1, \tag{A24}$$

$$\beta_L = \beta_R = 1/2, \quad \epsilon = 1/2, \tag{A25}$$

$$\alpha_L, \alpha_R \geq \max\left(\frac{2\mu}{4\gamma\Delta x}, \frac{2(\lambda + 2\mu)}{4\gamma\Delta x}\right), \tag{A26}$$

where the parameter γ is a constant depending on the order of accuracy of the method ($\gamma = 1/2$ for the second-order accurate methods we consider), then the semidiscrete energy estimate (18) is obtained.

Appendix B: Boundary Conditions and Penalty Terms for Section 3

For the continuous equations (19), on side (1) we impose the boundary conditions

$$\text{(bottom) } u^{(1)}(t, x, -L_y/2) = g_B^{(1)}(t, x), \tag{B1}$$

$$w^{(1)}(t, x, -L_y/2) = h_B^{(1)}(t, x), \quad x \in [0, L_x], \tag{B2}$$

$$\text{(periodic at left/right) } u^{(1)}(t, L_x, y) - u^{(1)}(t, 0, y) = 0, \quad y \in [-L_y/2, 0], \tag{B3}$$

$$w^{(1)}(t, L_x, y) - w^{(1)}(t, 0, y) = 0, \quad y \in [-L_y/2, 0], \tag{B4}$$

$$\sigma_{xx}^{(1)}(t, L_x, y) - \sigma_{xx}^{(1)}(t, 0, y) = 0, \quad y \in [-L_y/2, 0], \tag{B5}$$

$$\sigma_{xy}^{(1)}(t, L_x, y) - \sigma_{xy}^{(1)}(t, 0, y) = 0, \quad y \in [-L_y/2, 0]. \tag{B6}$$

On side (2) we impose

$$\text{(top) } u^{(2)}(t, x, L_y/2) = g_T^{(2)}(t, x), \tag{B7}$$

$$w^{(2)}(t, x, L_y/2) = h_T^{(2)}(t, x), \quad x \in [0, L_x], \tag{B8}$$

$$\text{(periodic at left/right) } u^{(2)}(t, L_x, y) - u^{(2)}(t, 0, y) = 0, \quad y \in [0, L_y/2], \tag{B9}$$

$$w^{(2)}(t, L_x, y) - w^{(2)}(t, 0, y) - 0 = 0, \quad y \in [0, L_y/2], \tag{B10}$$

$$\sigma_{xx}^{(2)}(t, L_x, y) - \sigma_{xx}^{(2)}(t, 0, y) = 0, \quad y \in [0, L_y/2], \tag{B11}$$

$$\sigma_{xy}^{(2)}(t, L_x, y) - \sigma_{xy}^{(2)}(t, 0, y) = 0, \quad y \in [0, L_y/2]. \tag{B12}$$

Taking the time derivative of (22) yields

$$\dot{E}^{(l)} = \int_{\Omega^{(l)}} \rho(u_t^{(l)} u_{tt}^{(l)} + w_t^{(l)} w_{tt}^{(l)}) + \frac{\mathrm{d}}{\mathrm{d}t}\left[\frac{1}{4\mu^{(l)}}\sigma_{ij}^{(l)}\left(\sigma_{ij}^{(l)} - \frac{\lambda^{(l)}}{3\lambda^{(l)} + 2\mu^{(l)}}\sigma_{kk}^{(l)}\delta_{ij}\right)\right] \mathrm{d}x\,\mathrm{d}y. \tag{B13}$$

Substituting the governing equations into (B13) and integrating by parts, all terms cancel except those on the boundary/interface:

$$\dot{E} = \int_{-L_y/2}^{0} u_t^{(1)} \sigma_{xx}^{(1)} \Big|_0^{L_x} dy + \int_0^{L_x} u_t^{(1)} \sigma_{xy}^{(1)} \Big|_{-L_y/2}^{0} dx + \int_{-L_y/2}^{0} w_t^{(1)} \sigma_{xy}^{(1)} \Big|_0^{L_x} dy + \int_0^{L_x} w_t^{(1)} \sigma_{yy}^{(1)} \Big|_{-L_y/2}^{0} dx$$
$$+ \int_0^{L_y/2} u_t^{(2)} \sigma_{xx}^{(2)} \Big|_0^{L_x} dy + \int_0^{L_x} u_t^{(2)} \sigma_{xy}^{(2)} \Big|_0^{L_y/2} dx + \int_0^{L_y/2} w_t^{(2)} \sigma_{xy}^{(2)} \Big|_0^{L_x} dy + \int_0^{L_x} w_t^{(2)} \sigma_{yy}^{(2)} \Big|_0^{L_y/2} dx. \tag{B14}$$

As done in section 2.1, for the sake of analysis we may take the boundary data in to zero, reducing (B14) to

$$\dot{E} = \int_0^{L_x} u_t^{(1)} \sigma_{xy}^{(1)} \Big|_0 + w_t^{(1)} \sigma_{yy}^{(a)} \Big|_0 - u_t^{(2)} \sigma_{xy}^{(2)} \Big|_0 - w_t^{(2)} \sigma_{yy}^{(2)} \Big|_0 \, dx. \tag{B15}$$

Taking the interface data $g_F = h_F = 0$ allows us to further simplify to

$$\dot{E} = \int_0^{L_x} -(g_F)_t \, \sigma_{xy} \Big|_0 - (h_F)_t \, \sigma_{yy} \Big|_0 \, dx = 0 \tag{B16}$$

where $\sigma_{xy} = \sigma_{xy}^{(1)} = \sigma_{xy}^{(2)}$ and $\sigma_{yy} = \sigma_{yy}^{(1)} = \sigma_{yy}^{(2)}$ are the common values at the interface.

For the semidiscrete equations (24), the discretized version of interface conditions (20) are given by

$$\text{(jump conditions)} \quad \mathbf{u}_B^{(2)} - \mathbf{u}_T^{(1)} = \mathbf{g}_F, \tag{B17}$$

$$\mathbf{w}_B^{(2)} - \mathbf{w}_T^{(1)} = \mathbf{h}_F, \tag{B18}$$

$$\text{(continuity conditions)} \quad [\tilde{\mathbf{T}}_x^{(1)}]_T - [\tilde{\mathbf{T}}_x^{(2)}]_B = 0, \tag{B19}$$

$$[\tilde{\mathbf{T}}_y^{(1)}]_T - [\tilde{\mathbf{T}}_y^{(2)}]_B = 0, \tag{B20}$$

where the components of the discrete traction vector at the fault interface are denoted by

$$\tilde{\mathbf{T}}_x^{(l)} = \mu^{(l)}(\mathbf{I} \otimes \mathbf{S})\mathbf{u}^{(l)} + \mu^{(l)}(\mathbf{D} \otimes \mathbf{I})\mathbf{w}^{(l)} \tag{B21}$$

$$\tilde{\mathbf{T}}_y^{(l)} = \lambda^{(l)}(\mathbf{D} \otimes \mathbf{I})\mathbf{u}^{(l)} + (\lambda^{(l)} + 2\mu^{(l)})(\mathbf{I} \otimes \mathbf{S})\mathbf{w}^{(l)}, \quad l = 1, 2. \tag{B22}$$

Using the superscripts d_1 and d_2 to denote enforcement of boundary conditions on displacements and s_1 and s_2 to denote those on tractions (stresses), respectively, the penalty vectors in equation (24) are given by

$$\mathbf{P}_1^{(1)} = \mathbf{p}_B^{(1),d_1} + \mathbf{p}_L^{(1),s_1} + \mathbf{p}_R^{(1),s_1} + \mathbf{p}_L^{(1),d_1} + \mathbf{p}_R^{(1),d_1} + \mathbf{p}_F^{(1),d_1} + \mathbf{p}_F^{(1),s_1} \tag{B23}$$

$$\mathbf{P}_2^{(1)} = \mathbf{p}_B^{(1),d_2} + \mathbf{p}_L^{(1),s_2} + \mathbf{p}_R^{(1),s_2} + \mathbf{p}_L^{(1),d_2} + \mathbf{p}_R^{(1),d_2} + \mathbf{p}_F^{(1),d_2} + \mathbf{p}_F^{(1),s_2} \tag{B24}$$

$$\mathbf{P}_1^{(2)} = \mathbf{p}_T^{(2),d_1} + \mathbf{p}_L^{(2),s_1} + \mathbf{p}_R^{(2),s_1} + \mathbf{p}_L^{(2),d_1} + \mathbf{p}_R^{(2),d_1} + \mathbf{p}_F^{(2),d_1} + \mathbf{p}_F^{(2),s_1} \tag{B25}$$

$$\mathbf{P}_2^{(2)} = \mathbf{p}_T^{(2),d_2} + \mathbf{p}_L^{(2),s_2} + \mathbf{p}_R^{(2),s_2} + \mathbf{p}_L^{(2),d_2} + \mathbf{p}_R^{(2),d_2} + \mathbf{p}_F^{(2),d_2} + \mathbf{p}_F^{(2),s_2} \tag{B26}$$

where vectors $\mathbf{p}$ with subscript B, T, L, and R impose the boundary conditions weakly (as in section 2.2) and those with subscript F enforce the fault interface conditions weakly. To enforce the boundary conditions in each subdomain, the penalty terms are given by

$$\mathbf{p}_B^{(1),d_1} = \alpha_B \mu^{(1)}(\mathbf{I} \otimes \mathbf{H}^{-1})\tilde{\mathbf{E}}_B(\mathbf{u}_B^{(1)} - \mathbf{g}_B^{(1)}) - \beta(\mathbf{I} \otimes \mathbf{H}^{-1})[\mu^{(1)}(\mathbf{I} \otimes \mathbf{S}^T)]\tilde{\mathbf{E}}_B(\mathbf{u}_B^{(1)} - \mathbf{g}_B^{(1)}) \tag{B27}$$

$$- \beta(\mathbf{I} \otimes \mathbf{H}^{-1})[\lambda^{(1)}(\mathbf{D}^T \otimes \mathbf{I})]\tilde{\mathbf{E}}_B(\mathbf{w}_B^{(1)} - \mathbf{h}_B^{(1)}) \tag{B28}$$

$$\mathbf{p}_L^{(1),d_1} = -\alpha_L(\mathbf{H}^{-1} \otimes \mathbf{I})\tilde{\mathbf{E}}_L(-\mathbf{u}_R^{(1)} + \mathbf{u}_L^{(1)}) + \beta_L(\mathbf{H}^{-1} \otimes \mathbf{I})\left[c^{(a)}(\mathbf{S}^T \otimes \mathbf{I})\right]\mathbf{E}_L(\mathbf{u}_R^{(1)} - \mathbf{u}_L^{(1)}) \tag{B29}$$

$$+ \beta_L(\mathbf{H}^{-1} \otimes \mathbf{I})\left[\mu^{(1)}(\mathbf{I} \otimes \mathbf{D}^T)\right]\mathbf{E}_L(\mathbf{w}_R^{(1)} - \mathbf{w}_L^{(1)}) \tag{B30}$$

$$\mathbf{p}_R^{(1),d_1} = -\alpha_R(\mathbf{H}^{-1} \otimes \mathbf{I})\tilde{\mathbf{E}}_R(\mathbf{u}_R^{(1)} - \mathbf{u}_L^{(1)}) + \beta_R(\mathbf{H}^{-1} \otimes \mathbf{I})\left[c^{(1)}(\mathbf{S}^T \otimes \mathbf{I})\right]\tilde{\mathbf{E}}_R(\mathbf{u}_R^{(1)} - \mathbf{u}_L^{(1)}) \tag{B31}$$

$$+ \beta_R(\mathbf{H}^{-1} \otimes \mathbf{I})\left[\mu^{(1)}(\mathbf{I} \otimes \mathbf{D}^T)\right]\tilde{\mathbf{E}}_R(\mathbf{w}_R^{(1)} - \mathbf{w}_L^{(1)}) \tag{B32}$$

$$\mathbf{p}_L^{(1),s_1} = -\epsilon(\mathbf{H}^{-1} \otimes \mathbf{I})\tilde{\mathbf{E}}_L\left([\mathbf{T}_x]_R^{(1)} - [\mathbf{T}_x]_L^{1)}\right) \tag{B33}$$

$$\mathbf{p}_R^{(1),s_1} = -\epsilon(\mathbf{H}^{-1} \otimes \mathbf{I})\tilde{\mathbf{E}}_R\left([\mathbf{T}_x]_R^{(1)} - [\mathbf{T}_x]_L^{(1)}\right) \tag{B34}$$

and

$$\mathbf{p}_T^{(2),d_2} = \alpha_T(\lambda^{(2)} + 2\mu^{(2)})(\mathbf{I} \otimes \mathbf{H}^{-1})\tilde{\mathbf{E}}_T(\mathbf{w}_T^{(2)} - \mathbf{h}_T^{(2)}) + \beta(\mathbf{I} \otimes \mathbf{H}^{-1})[(\lambda^{(2)} + 2\mu^{(b)})(\mathbf{I} \otimes \mathbf{S}^T)]\tilde{\mathbf{E}}_T(\mathbf{u}_T^{(2)} - \mathbf{g}_T^{(2)}) \tag{B35}$$

$$+ \beta(\mathbf{I} \otimes \mathbf{H}^{-1})[\mu^{(2)}(\mathbf{D}^T \otimes \mathbf{I})]\tilde{\mathbf{E}}_T(\mathbf{w}_T^{(2)} - \mathbf{h}_B^{(2)}) \tag{B36}$$

$$\mathbf{p}_L^{(2),d_2} = -\alpha_L(\mathbf{H}^{-1} \otimes \mathbf{I})\tilde{\mathbf{E}}_L(-\mathbf{w}_R^{(2)} + \mathbf{w}_L^{(2)}) + \beta_L(\mathbf{H}^{-1} \otimes \mathbf{I})\left[\mu^{(2)}(\mathbf{S}^T \otimes \mathbf{I})\right]\tilde{\mathbf{E}}_L(\mathbf{w}_R^{(2)} - \mathbf{w}_L^{(2)}) \tag{B37}$$

$$+ \beta_L(\mathbf{H}^{-1} \otimes \mathbf{I})\left[\lambda^{(2)}(\mathbf{I} \otimes \mathbf{D}^T)\right]\tilde{\mathbf{E}}_L(\mathbf{u}_R^{(2)} - \mathbf{u}_L^{(2)}) \tag{B38}$$

$$\mathbf{p}_R^{(2),d_2} = -\alpha_R(\mathbf{H}^{-1} \otimes \mathbf{I})\tilde{\mathbf{E}}_R(\mathbf{w}_R^{(2)} - \mathbf{w}_L^{(2)}) + \beta_R(\mathbf{H}^{-1} \otimes \mathbf{I})\left[\mu^{(2)}(\mathbf{S}^T \otimes \mathbf{I})\right]\tilde{\mathbf{E}}_R(\mathbf{w}_R^{(2)} - \mathbf{w}_L^{(2)}) \tag{B39}$$

$$+ \beta_R(\mathbf{H}^{-1} \otimes \mathbf{I})\left[\lambda^{(2)}(\mathbf{I} \otimes \mathbf{D}^T)\right]\tilde{\mathbf{E}}_R(\mathbf{u}_R^{(2)} - \mathbf{u}_L^{(2)}) \tag{B40}$$

$$\mathbf{p}_L^{(2),s_2} = -\epsilon(\mathbf{H}^{-1} \otimes \mathbf{I})\tilde{\mathbf{E}}_L\left([\mathbf{T}_y]_R^{(2)} - [\mathbf{T}_y]_L^{(2)}\right) \tag{B41}$$

$$\mathbf{p}_R^{(2),s_2} = -\epsilon(\mathbf{H}^{-1} \otimes \mathbf{I})\tilde{\mathbf{E}}_R\left([\mathbf{T}_y]_R^{(2)} - [\mathbf{T}_y]_L^{(2)}\right) \tag{B42}$$

where

$$\mathbf{T}_x^{(l)} = (\lambda^{(l)} + 2\mu^{(l)})(\mathbf{S} \otimes \mathbf{I})\mathbf{u}^{(l)} + \lambda^{(l)}(\mathbf{I} \otimes \mathbf{D})\mathbf{w}^{(l)} \tag{B43}$$

$$\mathbf{T}_y^{(l)} = \mu^{(l)}[(\mathbf{I} \otimes \mathbf{D})\mathbf{u}^{(l)} + (\mathbf{S} \otimes \mathbf{I})\mathbf{w}^{(l)}], \quad l = 1, 2. \tag{B44}$$

On side (1) the penalty vectors enforcing the interface conditions are

$$\mathbf{p}_F^{(1),d_1} = -\alpha_F(\mathbf{I} \otimes \mathbf{H}^{-1})\tilde{\mathbf{E}}_T\left(\mathbf{u}_T^{(1)} - \mathbf{u}_B^{(2)} + \mathbf{g}_F\right) + \beta_F(\mathbf{I} \otimes \mathbf{H}^{-1})[\mu^{(1)}(\mathbf{I} \otimes \mathbf{S}^T)]\tilde{\mathbf{E}}_T\left(\mathbf{u}_T^{(1)} - \mathbf{u}_B^{(2)} + \mathbf{g}_F\right)$$
$$+ \beta_F(\mathbf{I} \otimes \mathbf{H}^{-1})[\lambda^{(1)}(\mathbf{D}^T \otimes \mathbf{I})]\tilde{\mathbf{E}}_T\left(\mathbf{w}_T^{(1)} - \mathbf{w}_B^{(2)} + \mathbf{h}_F\right), \tag{B45}$$
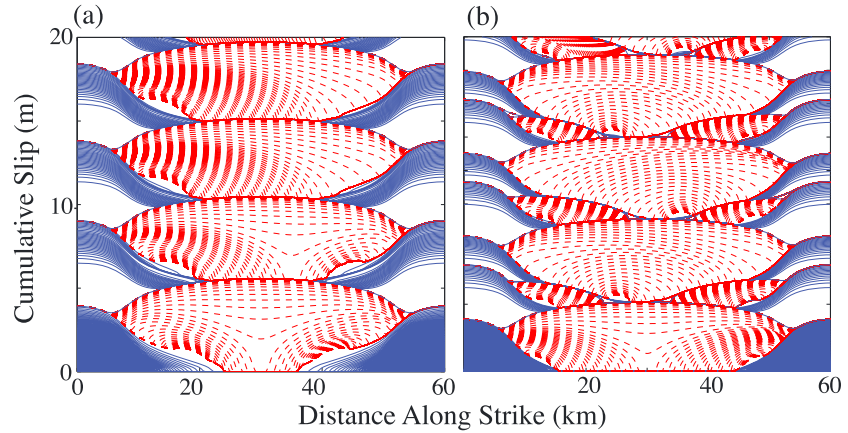
Figure C1. Grid refinement tests for the monomaterial simulations where twice as many grid points are used ($\Delta x = \Delta y = L_b/6$). (a) Slip profiles for the monomaterial problem with $D_c = 16$ mm (compare to Figure 5a) and for (b) $D_c = 8$ mm (compare to Figure 6a). The results appear identical.

$$\mathbf{p}_F^{(1),d_2} = -\alpha_F(\mathbf{I} \otimes \mathbf{H}^{-1})\tilde{\mathbf{E}}_T\left(\mathbf{w}_T^{(1)} - \mathbf{w}_B^{(2)} + \mathbf{h}_F\right) + \beta_F(\mathbf{I} \otimes \mathbf{H}^{-1})[(\lambda^{(1)} + 2\mu^{(1)})(\mathbf{I} \otimes \mathbf{S}^T)]\tilde{\mathbf{E}}_T\left(\mathbf{w}_T^{(1)} - \mathbf{w}_B^{(2)} + \mathbf{h}_F\right)$$
$$+ \beta_F(\mathbf{I} \otimes \mathbf{H}^{-1})[\mu^{(1)}(\mathbf{D}^T \otimes \mathbf{I})]\tilde{\mathbf{E}}_T\left(\mathbf{u}_T^{(1)} - \mathbf{u}_B^{(2)} + \mathbf{g}_F\right),$$

(B46)

$$\mathbf{p}_F^{(1),s_1} = -\epsilon_F(\mathbf{I} \otimes \mathbf{H}^{-1})\tilde{\mathbf{E}}_T\left([\tilde{\mathbf{T}}_x^{(1)}]_T - [\tilde{\mathbf{T}}_x^{(2)}]_B - 0\right),$$

(B47)

$$\mathbf{p}_F^{(1),s_2} = -\epsilon_F(\mathbf{I} \otimes \mathbf{H}^{-1})\tilde{\mathbf{E}}_T\left([\tilde{\mathbf{T}}_y^{(1)}]_T - [\tilde{\mathbf{T}}_y^{(2)}]_B - 0\right),$$

(B48)

and on side (2) we have

$$\mathbf{p}_F^{(2),d_1} = -\alpha_F(\mathbf{I} \otimes \mathbf{H}^{-1})\tilde{\mathbf{E}}_B\left(-\mathbf{u}_T^{(1)} + \mathbf{u}_B^{(2)} - \mathbf{g}_F\right) + \beta_F(\mathbf{I} \otimes \mathbf{H}^{-1})[\mu^{(2)}(\mathbf{I} \otimes \mathbf{S}^T)]\tilde{\mathbf{E}}_B\left(\mathbf{u}_T^{(1)} - \mathbf{u}_B^{(2)} + \mathbf{g}_F\right)$$
$$+ \beta_F(\mathbf{I} \otimes \mathbf{H}^{-1})[\lambda^{(2)}(\mathbf{D}^T \otimes \mathbf{I})]\tilde{\mathbf{E}}_B\left(\mathbf{w}_T^{(1)} - \mathbf{w}_B^{(2)} + \mathbf{h}_F\right),$$

(B49)

$$\mathbf{p}_F^{(2),d_2} = -\alpha_F(\mathbf{I} \otimes \mathbf{H}^{-1})\tilde{\mathbf{E}}_B\left(-\mathbf{w}_T^{(1)} + \mathbf{w}_B^{(2)} - \mathbf{h}_F\right) + \beta_F(\mathbf{I} \otimes \mathbf{H}^{-1})[(\lambda^{(2)} + 2\mu^{(b)})(\mathbf{I} \otimes \mathbf{S}^T)]\tilde{\mathbf{E}}_B\left(\mathbf{w}_T^{(1)} - \mathbf{w}_B^{(2)} + \mathbf{h}_F\right)$$
$$+ \beta_F(\mathbf{I} \otimes \mathbf{H}^{-1})[\mu^{(2)}(\mathbf{D}^T \otimes \mathbf{I})]\tilde{\mathbf{E}}_B\left(\mathbf{u}_T^{(1)} - \mathbf{u}_B^{(2)} + \mathbf{g}_F\right),$$

(B50)

$$\mathbf{p}_F^{(2),s_1} = -\epsilon_F(\mathbf{I} \otimes \mathbf{H}^{-1})\tilde{\mathbf{E}}_B\left([\tilde{\mathbf{T}}_x^{(1)}]_T - [\tilde{\mathbf{T}}_x^{(2)}]_B - 0\right),$$

(B51)

and

$$\mathbf{p}_F^{(2),s_2} = -\epsilon_F(\mathbf{I} \otimes \mathbf{H}^{-1})\tilde{\mathbf{E}}_B\left([\tilde{\mathbf{T}}_y^{(1)}]_T - [\tilde{\mathbf{T}}_y^{(2)}]_B - 0\right).$$

(B52)

The penalty parameters $\alpha_T, \alpha_B, \beta, \beta_L, \beta_R$, and ϵ are given in Appendix A. *Duru and Virta* [2014] show that if the remaining penalty parameters satisfy

$$\alpha_F \geq \max\left(\frac{\mu^{(1)} + \mu^{(2)}}{4\gamma\Delta y}, \frac{(\lambda^{(1)} + 2\mu^{(1)}) + (\lambda^{(2)} + 2\mu^{(2)})}{4\gamma\Delta y}\right),$$

(B53)

$$\beta_F = 1/2, \quad \epsilon_F = 1/2,$$

(B54)

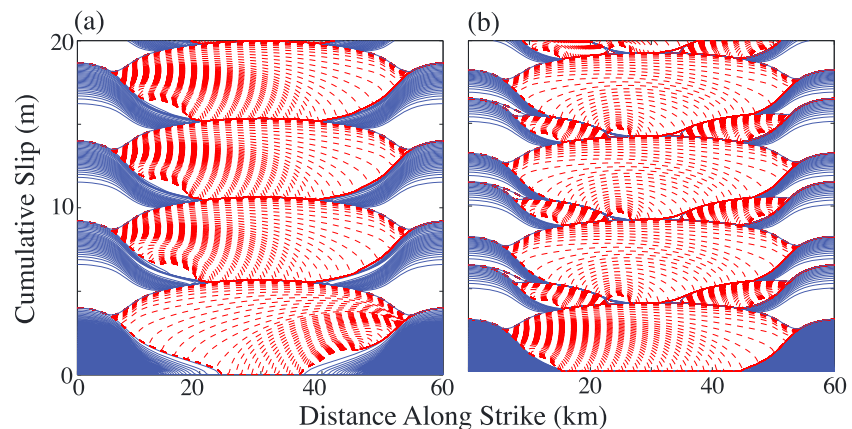then the semidiscrete energy estimate (26) is obtained.

Figure C2. Grid refinement tests for the bimaterial simulations with 5% contrast, where twice as many grid points are used ($\Delta x = \Delta y = L_b/6$). (a) Slip profiles for the bimaterial problem with $D_c = 16$ mm (compare to Figure 7a) and for (b) $D_c = 8$ mm (compare to Figure 8a). The results appear identical.

Appendix C: Grid Refinement Tests and Regularized Normal Stress Response

To check that our resolution is sufficient, we do two grid refinement tests with twice as many grid points ($L_b/dx = 6$). Figures C1 and C2 show the results from two monomaterial simulations and two bimaterial simulations, each with $D_c = 16$ and 8 mm. The results appear identical to those on a coarser grid, which suggest that our resolution is adequate.

In the context of steady sliding of bimaterial half spaces with Coulomb friction, *Ranjith and Rice* [2001] showed that the problem is ill posed for a wide range of friction coefficients and that solutions fail to converge with mesh refinement. By introducing a regularization of friction to have a memory of normal stress history, convergence is recovered [*Ranjith and Rice*, 2001; *Cochard and Rice*, 2000]. *Rice et al.* [2001] extend this to the quasi-static analysis for rate-and-state friction on an interface separating dissimilar material and show that the problem is well posed if the direct effect parameter a is positive. Although our simulations are quasi-dynamic, we suspect that well posedness still holds. Thus, we do not included a normal stress response in our simulations, and our grid refinement tests suggest that our solutions are converging with mesh refinement, see Figures C1 and C2. To test this theory, however, we include the normal stress response (a particular case from *Ampuero and Ben-Zion* [2008] and *Shi and Day* [2013]) by introducing a second state variable σ^* that has the steady state value equal to the effective normal stress on the fault. Letting $\boldsymbol{\sigma}^*$ denote the discrete grid vector approximating σ^*, time step 6 in section 5 is altered so that equation (41) is replaced with

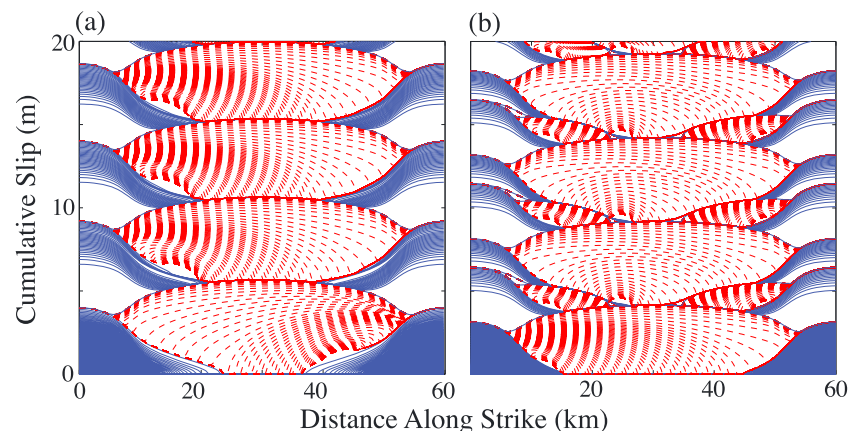$$\tau^n - \eta V^n = \sigma^{*,n} f(V^n, \psi^n) \tag{C1}$$

Figure C3. Simulation results when adding a normal stress regularization to the bimaterial simulations with 5% contrast. (a) Slip profiles for the bimaterial problem with $D_c = 16$ mm (compare to Figure 7a) and for (b) $D_c = 8$ mm (compare to Figure 8a). The results appear identical.

and σ^* evolves according to

$$\dot{\sigma}^* = -\frac{V}{D_c}\left[\sigma^* - \sigma\right].$$

(C2)

Results from these simulations are shown in Figure C3. Compared to their respective counterparts that were done without the regularization (Figures 7a) and 8a), the results appear identical.

References

Adams, G. G. (1995), Self-excited oscillations of two elastic half-spaces sliding with constant coefficient of friction, *J. Appl. Mech.*, *62*, 867–872.

Allam, A. A., Y. Ben-Zion, and Z. Peng (2014), Seismic imaging of a bimaterial interface along the Hayward fault, CA, with fault zone head waves and direct P arrivals, *Pure Appl. Geophys.*, *171*, 2993–3011, doi:10.1007/s00024-014-0784-0.

Ampuero, J.-P., and Y. Ben-Zion (2008), Cracks, pulses and macroscopic asymmetry of dynamic rupture on a bimaterial interface with velocity-weakening friction, *Geophys. J. Int.*, *173*, 674–692.

Ampuero, J.-P., and A. M. Rubin (2008), Earthquake nucleation on rate and state faults: Aging and slip laws, *J. Geophys. Res.*, *113*, B01302, doi:10.1029/2007JB005082.

Andrews, D. J., and Y. Ben-Zion (1997), Wrinkle-like slip pulse on a fault between different materials, *J. Geophys. Res.*, *102*(B1), 553–571, doi:10.1029/96JB02856.

Andrews, D. J., and R. A. Harris (2005), The wrinkle-like slip pulse is not important in earthquake dynamics, *Geophys. Res. Lett.*, *32*, L23303, doi:10.1029/2005GL023996.

Anooshehpoor, A., and J. Brune (1999), Wrinkle-like Weertman pulse at the interface between two blocks of foam rubber with different velocities, *Geophys. Res. Lett.*, *26*, 2025–2028.

Ben-Zion, Y., and D. J. Andrews (1998), Properties and implications of dynamic rupture along a material interface, *Bull. Seismol. Soc. Am.*, *88*, 1085–1094.

Ben-Zion, Y., and Y. Huang (2002), Dynamic rupture on an interface between a compliant fault zone layer and a stiffer surrounding solid, *J. Geophys. Res.*, *107*(B2), 2042, doi:10.1029/2001JB000254.

Ben-Zion, Y. (2006), Comment on "Material contrast does not predict earthquake rupture propagation direction" by R. A. Harris and S. M. Day, *Geophys. Res. Lett.*, *33*, L13310, doi:10.1029/2005GL025652.

Bennington, N. L., C. Thurber, Z. Peng, H. Zhang, and P. Zhao (2013), Incorporating fault zone head wave and direct wave secondary arrival times into seismic tomography: Application at Parkfield, California, *J. Geophys. Res. Solid Earth*, *118*, 1008–1014, doi:10.1002/jgrb.50072.

Brietzke, G. B., A. Cochard, and H. Igel (2009), Importance of bimaterial interfaces for earthquake dynamics and strong ground motion, *Geophys. J. Int.*, *178*, 921–938.

Chéry, J. (2008), Geodetic strain rate across the San Andreas fault reflects elastic plate thickness variations (rather than fault slip rate), *Earth Planet. Sci. Lett.*, *269*, 352–365.

Cochard, A., and J. R. Rice (2000), Fault rupture between dissimilar materials: Ill-posedness, regularizaion, and slip-pulse response, *J. Geophys. Res.*, *105*(B11), 25,891–25,907.

Dalguer, L. A., and S. M. Day (2009), Asymmetric rupture of large aspect-ratio faults at bimaterial interface in 3D, *Geophys. Res. Lett.*, *36*, L23307, doi:10.1029/2009GL040303.

Danesi, S., S. Bannister, and A. Morelli (2007), Repeating earthquakes from rupture of an asperity under an Antarctic outlet glacier, *Earth Planet. Sci. Lett.*, *253*, 151–158.

DeDontney, N., E. L. Templeton-Barrett, J. R. Rice, and R. Dmowska (2011), Influence of plastic deformation on bimaterial fault rupture directivity, *J. Geophys. Res.*, *116*, B10312, doi:10.1029/2011JB008417.

Dieterich, J. H. (1979), Modeling of rock friction: 1. Experimental results and constitutive equations, *J. Geophys. Res.*, *84*, 2161–2168.

Dor, O., T. K. Rockwell, and Y. Ben-Zion (2006), Geological observations of damage asymmetry in the structure of the San Jacinto, San Andreas and Punchbowl faults in southern California: A possible indicator for preferred rupture propagation direction, *Pure Appl. Geophys.*, *163*, 301–349.

Dor, O., C. Yildirim, T. K. Rockwell, Y. Ben-Zion, O. Emre, M. Sisk, and T. Y. Duman (2008), Geological and geomorphologic asymmetry across the rupture zones of the 1943 and 1944 earthquakes on the North Anatolian Fault: Possible signals for preferred earthquake propagation direction, *Geophys. J. Int.*, *173*, 483–504.

Duan, B. (2008), Asymmetric off-fault damage generated by bilateral ruptures along a bimaterial interface, *Geophys. Res. Lett.*, *35*, L14306, doi:10.1029/2008GL034797.

Duru, K., and K. Virta (2014), Stable and high order accurate difference methods for the elastic wave equation in discontinuous media, *J. Comput. Phys.*, *279*, 37–62, doi:10.1016/j.jcp.2014.08.046.

Erickson, B. A., and E. M. Dunham (2014), An efficient numerical method for earthquake cycles in heterogeneous media: Alternating subbasin and surface-rupturing events on faults crossing a sedimentary basin, *J. Geophys. Res. Solid Earth*, *119*, 3290–3316, doi:10.1002/2013JB010614.

Fialko, Y. (2006), Interseismic strain accumulation and the earthquake potential on the southern San Andreas fault system, *Nature*, *441*, 968–971.

Harris, R. A., and S. M. Day (1997), Effects of a low-velocity zone on a dynamic rupture, *Bull. Seismol. Soc. Am.*, *87*, 1267–1280.

Harris, R. A., and S. M. Day (2005), Material contrast does not predict earthquake rupture propagation direction, *Geophys. Res. Lett.*, *32*, L23301, doi:10.1029/2005GL023941.

Harris, R. A., and S. M. Day (2006), Reply to comment by Y. Ben-Zion on "Material contrast does not predict earthquake rupture propagation direction", *Geophys. Res. Lett.*, *33*, L13311, doi:10.1029/2006GL026811.

Kane, D. L., P. M. Shearer, B. P. Goertz-Allmann, and F. L. Vernon (2013), Rupture directivity of small earthquakes at Parkfield, *J. Geophys. Res. Solid Earth*, *118*, 212–221, doi:10.1029/2012JB009675.

Lapusta, N., J. R. Rice, Y. Ben-Zion, and G. Zheng (2000), Elastodynamic analysis for slow tectonic loading with spontaneous rupture episodes on faults with rate-and-state dependent friction, *J. Geophys. Res.*, *105*(B10), 23,765–23,789.

Lapusta, N., and J. R. Rice (2003), Nucleation and early seismic propagation of small and large events in a crustal earthquake model, *J. Geophys. Res.*, *108*(B4), 2205, doi:10.1029/2001JB000793.

Lapusta, N., and Y. Liu (2009), Three-dimensional boundary integral modeling of spontaneous earthquake sequences and aseismic slip, *J. Geophys. Res.*, *114*, B09303, doi:10.1029/2008JB005934.

Le Pichon, X., C. Kreemer, and N. Chamot-Rooke (2005), Asymmetry in elastic properties and the evolution of large continental strike-slip faults, *J. Geophys. Res.*, *110*(B3), B03405, doi:10.1029/2004JB003343.

Marone, C. (1998), Laboratory-derived friction laws and their application to seismic faulting, *Annu. Rev. Earth Planet. Sci.*, *26*, 643–696.

Mattsson, K., and J. Nordström (2004), Summation by parts operators for finite difference approximations of second derivatives, *J. Comput. Phys.*, *199*(2004), 503–540.

Mattsson, K. (2011), Summation by parts operators for finite difference approximations of second-derivatives with variable coefficients, *J. Sci. Comput.*, *51*, 650–682.

Ranjith, K., and J. R. Rice (2001), Slip dynamics at an interface between dissimilar materials, *J. Mech. Phys. Solids*, *49*, 341–361.

Rice, J. R., and A. L. Ruina (1983), Stability of steady-frictional slipping, *J. Appl. Mech.*, *50*, 343–349.

Rice, J. R. (1993), Spatio-temporal complexity of slip on a fault, *J. Geophys. Res.*, *98*, 9985–9907.

Rice, J. R., N. Lapusta, and K. Ranjith (2001), Rate and state dependent friction and the stability of sliding between elastically deformable solids, *J. Mech. Phys. Solids*, *49*, 1865–1898.

Roache, P. (1998), *Verification and Validation in Computational Science and Engineering*, 1st ed., Hermosa Publ., Albuquerque, N. M.

Rubin, A. M., and D. Gillard (2000), Aftershock asymmetry/rupture directivity among central San Andreas fault microearthquakes, *J. Geophys. Res.*, *105*(B8), 19,09–19,109.

Rubin, A. M., and J.-P. Ampuero (2005), Earthquake nucleation on (aging) rate and state faults, *J. Geophys. Res.*, *110*, B11312, doi:10.1029/2005JB003686.

Rubin, A. M., and J.-P. Ampuero (2007), Aftershock asymmetry on a bimaterial interface, *J. Geophys. Res.*, *112*, B0530, doi:10.1029/2006JB004337.

Ruina, A. (1983), Slip instability and state variable friction laws, *J. Geophys. Res.*, *88*(B12), 10,359–10,370.

Shi, Z., and Y. Ben-Zion (2006), Dynamic rupture on a bimaterial interface governed by slip-weakening friction, *Geophys. J. Int.*, *165*(2), 469–484, doi:10.1111/j.1365-246X.2006.02853.x.

Shi, Z., and S. M. Day (2013), Rupture dynamics and ground motion from 3-D rough-fault simulations, *J. Geophys. Res. Solid Earth*, *118*, 1122–1141, doi:10.1002/jgrb.50094.

Thomas, M. Y., N. Lapusta, H. Noda, and J. P. Avouac (2014), Quasi-dynamic versus fully dynamic simulations of earthquakes and aseismic slip with and without enhanced coseismic weakening, *J. Geophys. Res. Solid Earth*, *119*, 1986–2004, doi:10.1002/2013JB010615.

Xia, K., A. J. Rosakis, H. Kanamori, and J. R. Rice (2005), Laboratory earthquakes along inhomogeneous faults: directionality and supershear, *Science*, *308*, 681–684.

Weertman, J. (1980), Unstable slippage across a fault that separates elastic media of different elastic constants, *J. Geophys. Res.*, *85*(B3), 1455–1461.

Weertman, J. (2005), Slip event propagation direction in transition region of low surface slope, *Ann. Glaciol.*, *40*, 43–46.

Zhao, P., Z. Peng, Z. Shi, M. Lewis, and Y. Ben-Zion (2010), Variations of the velocity contrast and rupture properties of M6 earthquakes along the Parkfield section of the San Andreas fault, *Geophys. J. Int.*, *180*, 765–780.